

# Retrospective Study of FinDer Algorithm During the 2019, Ridgecrest Earthquake Sequence

Wei Huang (✉ [250253758@qq.com](mailto:250253758@qq.com))

China Earthquake Administration Institute of Engineering Mechanics <https://orcid.org/0000-0001-8620-946X>

---

## Research Article

**Keywords:** earthquake early warning, FinDer, Ridgecrest earthquake sequence, simulated real-time alert performance, seismic risk mitigation.

**Posted Date:** November 10th, 2021

**DOI:** <https://doi.org/10.21203/rs.3.rs-1009668/v1>

**License:**  This work is licensed under a Creative Commons Attribution 4.0 International License.

[Read Full License](#)

---

1

# Retrospective study of FinDer algorithm during the 2019, Ridgecrest earthquake sequence

2 **Wei Huang<sup>1\*</sup>**

3 <sup>1</sup>Institute of Engineering Mechanics, China Earthquake Administration, Harbin, China

4 **\* Correspondence:**

5 Wei Huang

6 hwcxr2008@126.com

7 **Keywords** earthquake early warning, FinDer, Ridgecrest earthquake sequence, simulated  
8 real-time alert performance, seismic risk mitigation.

## 9 **ABSTRACT**

10 Real-time characterization of evolving rupture is crucial for mitigating against  
11 seismic hazards exposed to potentially devastating earthquake events in EEWs  
12 (Earthquake Early Warning system). Currently, FinDer (Finite Fault Rupture Detector)  
13 algorithm explicitly utilizes observed ground motion pattern to solve for the evolving  
14 rupture to generate alerts for early warning purpose, which is currently contributing to  
15 ShakeAlert EEW system in West Coast of United States, within the area covered by the  
16 Advanced National Seismic System (ANSS) network. Here we implement FinDer offline  
17 to explore its feasibility assuming ideal field telemetry on a database of real earthquakes  
18 with magnitude  $M \geq 5.0$  occurring in Ridgecrest, Southern California in 2019. We  
19 specially focus on evaluating the performance of FinDer through end-user-orientated  
20 analysis in terms of warning time and accuracy of ground shaking prediction. Overall,  
21 FinDer classifies alerts with a rate of success over 74% across a broad range of alert  
22 criteria, substantial fraction of sites can be successfully alerted including the most difficult  
23 cases with high ground motion intensities regardless of invariable few seconds of warning  
24 time. FinDer can be configured to generate more useful alerts with higher cost savings by  
25 applying lower alert threshold during the Ridgecrest earthquake sequence. Furthermore,  
26 although large fractions of sites would have been timely alerted, it is significantly  
27 challenging for predicting accurately the moderate or worse intensities (Modified Mercalli  
28 Intensity  $> 5.5$ ) in advance even if applying lower alert threshold and higher damage  
29 threshold. Nonetheless, FinDer performs well in an evolutionary manner to guarantee  
30 reliable alerts by resorting to a consistent description of point source or occurring rupture.

## 31 **1 Introduction**

32 The 2019 Ridgecrest, Southern California, earthquake sequence mainly includes a  
33 Mw6.4 foreshock at 17:33 p.m. UTC on July 4, followed 34 hr later by a Mw7.1 event at  
34 03:19 a.m. on July 6. The devastating earthquake sequence occurred within the north  
35 Eastern California Shear Zone (ECSZ), filling the seismic gap between the 1872 Owens  
36 Valley surface rupture to the north and the 1992 Landers, 1999 Hector mine surface break  
37 to the south (Sieh et al. 1993; Hough & Hutton 2008). Previous geological and geodetic  
38 observations indicated that San Andreas fault and the ECSZ with a right-lateral slip rate of  
39 10-15 *mm/yr* accommodate comparable dextral shear motion between the Pacific and  
40 North American plates, the integrated deformation within northern ECSZ is partitioned on  
41 several NW-NNW trending parallel faults within Owens Valley, Panamint Valley and  
42 Southern Death Valley and the EW trending Garlock fault with sinistral motion (Dokka et  
43 al. 1990; Sauber et al. 1994; Miller et al. 2001) (Fig. 1a). In general, the Focal mechanisms  
44 for the total earthquake sequence feature predominantly strike slip, either on a NW-SE or  
45 SW-NE plane (USGS 2019, see data and source). Field investigations indicated that the  
46  $M_w$ 6.4 event surface rupture extended 18 km along a left-lateral NE-trending fault near the  
47 Garlock fault to the south (Stewart et al. 2019), but both foreshocks and aftershocks  
48 distribution of the  $M_w$ 6.4 event before Mw7.1 mainshock possibly involved two nearly  
49 orthogonal faults that oriented northwest and southwest (Ross et al. 2019; Shelly et al.  
50 2020). The  $M_w$ 7.1 rupture propagated bilaterally along a NW-trending fault over length of  
51 50 km characterized by dominantly right-lateral strike-slip motion (Stewart et al. 2019;  
52 DuRoss et al. 2020). Waveform inversions by both seismic and geodetic measurements  
53 reveal that the  $M_w$ 6.4 rupture nucleated on a northwest-striking subfault parallel to the  
54 mainshock rupture but propagated almost 20 km unilaterally toward SW for about 12s, the  
55 maximum slip mainly occurred along the southwest-striking fault strand, but the  
56 northwest-striking fault strand also exhibits a moderate slip (Ross et al. 2019; Chen et al.  
57 2019; Wang et al. 2020b). For the  $M_w$ 7.1 mainshock, Seismic and geodetic observations  
58 document 55 km of bilateral surface rupture along the NW trending fault strand for about  
59 22s (Ross et al. 2019; Barnhart 2019; Wang et al. 2020a). Seismological and Geodetic  
60 including InSAR measurements provide a comprehensive view of this earthquake  
61 sequence, suggesting that the sequence ruptured a highly segmented cross-faulting  
62 structure over a wide region with the characteristic of low rupture velocity and high  
63 aftershock productivity. This behavior corroborates the failure behavior of an immature  
64 fault zone (Ross et al. 2019; Barnhart et al. 2019; Liu et al. 2019).

65 EEW (Earthquake early warning) system contributes in identifying the potential  
66 seismic hazards and initiates the risk mitigation actions in real-time environment. This is  
67 mainly achieved by timely event detection and accurate characterization of earthquake  
68 source or growing rupture, and notification of expected imminent strong ground shaking  
69 in target regions around the source in advance. There currently exists various promising

70 seismic EEW systems or algorithms in phases of testing, developing and operation in  
71 earthquake-prone regions around the world. Virtual Seismologists has been applied in  
72 Switzerland (Cua & Heaton 2007; Massin et al. 2021), California (Cua et al. 2009a) and  
73 Patras, Greece (Sokos et al. 2016). PRESTo operates in Southern Italy (Satriano et al. 2010;  
74 Zollo et al. 2010; Piccozi et al. 2015), extending their application for Ibero-Maghrebian  
75 region, Spain (Carranza et al. 2017) and Greece (Bracale et al. 2021). Ground motion  
76 driven algorithm PLUM (the Propagation of local undamped motion) is currently  
77 implemented by JMA (Japan Meteorological Agency) in Japan (Kodera et al. 2016), and  
78 also tested in California (Cochran et al. 2018). ElarmS currently contributes to ShakeAlert  
79 in California (Chung et al., 2019), tested offline in Italy (Olivieri et al. 2008) and Israel  
80 (Nov et al. 2016). On-site approach has been exploited in California (Wu et al. 2007; Böse  
81 et al. 2009), Taiwan (Wu et al. 2005; Hsu et al. 2016) and also investigated in ISNet  
82 seismic network of Southern Italy (Caruso et al. 2017), Kyrgyzstan (Bindi et al. 2015;  
83 Parolai et al. 2015) and Israel (Sadeh et al. 2014). Gutenberg Algorithm (Meier et al. 2015)  
84 is also planned for application within ShakeAlert of California and SED (Swiss  
85 Seismological Service) at ETH Zürich. Recently, in California, the ShakeAlert EEW  
86 demonstration system exploits live data streamed by the dense seismic array (operated  
87 within Advanced National Seismic System (ANSS) network including 1115 contributing  
88 short-period, broadband and strong motion sensors until April, 2018) deployed across the  
89 West Coast of the United States's active seismogenic zones with different seismic hazard  
90 contexts (Cochran et al. 2018; Given et al. 2018; McGuire et al. 2021a). Since 2018,  
91 ShakeAlert integrates EPIC (Earthquake Point-Source Integrated Code) algorithms (Allen  
92 et al. 2007; Brown et al. 2011; Kuyuk et al. 2014; Chung et al. 2019) and FinDer algorithm  
93 (Böse et al. 2018) within ANSS, which is mainly coordinated by United States Geological  
94 Survey (USGS). EPIC provides the point source solution using the initial portion of P  
95 wave, and meanwhile, FinDer generates optimum finite source solution by resorting to  
96 high-frequency aspects of observed ground motion, the level and distribution of observed  
97 ground motion jointly contributes in providing the optimum solution for the evolving  
98 rupture (Böse et al. 2012, 2015, 2018). Suffered from magnitude saturation by traditional  
99 EEW algorithms, epicentral distance underpinned point-source algorithms is inadequate  
100 for characterizing the extended fault plane for moderate to large magnitudes ( $M \geq 6.0$ ) in  
101 the real earthquakes. FinDer has been demonstrated to be well suited to provide reliable  
102 and consistent source characterization over a wide range of magnitude events (Böse et al.  
103 2015; Böse et al. 2018). Rapid knowledge of derived fault rupture and the spatial slip  
104 distribution over the fault revealed from wide spectrum brings significant additions to  
105 magnitude estimation thus ground motion shaking forecast (Böse et al. 2018, 2021).

106 This article is arranged as follows. First, we examine the scientific feasibility of  
107 FinDer algorithm alone in even detection and source characterization during the 2019,  
108 Ridgecrest earthquake sequence. Second, FinDer are configured to predict the expected  
109 ground shaking at the monitoring sites to classify alerts by threshold based

110 end-user-orientated metric. Finally, we specially focus on evaluating the reliability of  
 111 FinDer alerts through warning time across a wide range of alert criteria. Therefore, we  
 112 identify the optimum alert criterion under which FinDer can achieve the best alert  
 113 performance, and the maximum possibilities the algorithm performance implying for  
 114 ground motion predictions especially for high intensities at proximal sites.

## 115 **2 Methodologies**

### 116 **2.1 FinDer**

117 FinDer extracts the essential high-frequency aspects of the waveforms from observed  
 118 ground motions, thereby associating the information of radiated energy within specific  
 119 seismic network with precalculated theoretical templates to solve for the optimum finite  
 120 fault model including magnitude that accounts for the dimension of finite fault implicitly,  
 121 and the orientation and the extent of fault rupture, which will continuously updates if the  
 122 evolving rupture is occurring (Böse et al. 2012, 2015). With contrast to the original version  
 123 of FinDer, in the new version of FinDer (also called FinDer v.2, Böse et al. 2018), the  
 124 series of template are precalculated according to the ground motion exceedance level  
 125 according to certain magnitude bin, which are also applied to generate the observed binary  
 126 image in real time (Böse et al. 2012). In fact, this implementation avoids the continuous  
 127 matching with more computation efficiency, meanwhile, FinDer is capable of identifying  
 128 the earthquake events within a broad range of magnitude size from either small events or  
 129 large events.

130 In this study, we generate template with spatial resolution of 1km following the  
 131 methods proposed by Böse et al. (2018), we adopt the GMPEs (Ground Motion Prediction  
 132 Equations) of Cua & Heaton (2009b) assuming rock condition and the magnitude-rupture  
 133 length scaling relationship of Well & Coppersmith (1994) as follows.

$$134 \quad T(x, y) = \log_{10}(\text{PGA}(x, y)) = [0.73M - 7.2 \times 10^{-4}(\sqrt{R^2 + 9} + C(M)) - 1.48 \times \log_{10}(\sqrt{R^2 + 9} + C(M)) - 0.42] + \log_{10}(1.1) \quad (1)$$

$$135 \quad C(M) = 1.16 \exp[0.96(M - 5)] \times [\arctan(M - 5) + \pi / 2] \quad (2)$$

$$136 \quad M = 1.49 \log_{10}(L) + 4.33 \quad (3)$$

137 In equation (1), R is regarded as Joyner-Boore distance(Rjb) measured in kilometers  
 138 if magnitude M is larger than 5.0. Magnitude M is converted from equation (3), PGA is  
 139 measured in  $cm/s^2$ . L in equation 3 represents the length of the fault rupture. Note that,  
 140  $\log_{10}(1.1)$  in equation (3) is a empirical tuning factor for converting root mean square of

141 peak ground amplitudes to the maximum of two horizontal components to be in line with  
142 the observed amplitudes (Cua & Heaton 2009b). The equation (3) is adopted for the  
143 earthquake sequence in this issue to be compatible with the tectonic regime of Southern  
144 California, where strike-slip ruptures dominate. We assume ground motions in the  
145 research region has covered different site conditions without applying site corrections as  
146 proposed by Böse et al. (2018).

## 147 **2.2 The MMI-threshold Alert Strategy**

148 In order to qualify the reliability of source characterization of FinDer from  
149 end-user-orientated perspective, we introduce the threshold based alert performance  
150 measured in MMI scale (Modified Mercalli Intensity) through warning time on a  
151 site-by-site basis. The MMI-threshold approach enables us to depict the classification in  
152 terms of both the timeliness and the accuracy of alerts. A alert will be released in  
153 operational EEW system if the predicted intensity is larger or equal to the predefined alert  
154 threshold regardless of whether the actual ground motion may be overestimated or  
155 underestimated eventually.

156 With respect to the classification of alerts, four categories are defined as follows  
157 according to alert threshold ( $MMI_{alert}$ ) and the damage threshold ( $MMI_{tw}$ ): (1) true positive  
158 alert (TP), when both the observed intensity and the predicted intensity exceed the alert  
159 threshold; (2) true negative alert (TN), if both the observed intensity and the predicted  
160 intensity are smaller than the alert threshold; (3) False positive alert (FP), if the measured  
161 intensity is smaller than the alert threshold but the predicted intensity exceeds the alert  
162 threshold; (4) False negative alert (FN), if the observed intensity reaches the alert  
163 threshold but the predicted intensity is smaller than the alert threshold, or the observed  
164 intensity has exceeded the damage threshold before the predicted intensity reaches the  
165 alert threshold. During the 2019 Ridgecrest earthquake sequence, according to the  
166 predefined threshold at each individual site, we can evaluate the reliability of FinDer to  
167 generate useful alerts through warning time. The warning time is defined as the time  
168 difference between the time the predicted intensity for the first time reaches the alert  
169 threshold and the time when the actual intensity exceeds the damage threshold. Indeed,  
170 warning time is approximately regarded as the time interval caused by the time gap  
171 between the move out speed and the velocity of theoretical S wave arrival in Figure 1c.  
172 Also fast algorithms help reducing EEW delays with fast move out speed (e.g., more than  
173 8 km/s for 2019, Ridgecrest earthquake sequence not including data latency). Therefore  
174 the warning time formula accounts for the EEW system's capability to quickly identify the  
175 source or rupture as it evolves, as well as on the level of shaking at which end users are  
176 expected to initiate corresponding mitigation actions.

## 177 **2.3 The Accuracy Evaluation Metric of Ground Motion Prediction**

178 To explore the maximum accuracy FinDer can achieve conditional on available  
179 warning time, we examine the ground motion prediction errors measuring in MMI scale  
180 through warning time. The ground motion prediction error is defined as the observed  
181 ground motion minus the corresponding prediction for each individual site (Meier et al.  
182 2017b; Böse et al. 2018). The warning time here is defined as the time until the actual  
183 ground motion exceeds the predefined damage level to initiate mitigation actions or  
184 theoretical S-wave arrival for sites with below-threshold ground motion (Minson et al.  
185 2018; Chung et al. 2020). Our concern in this result is not the specific value obtained for  
186 each individual estimate but rather on the overall trend or accuracy on average in the  
187 ground motion domain (Meier et al. 2017b).

### 188 **3 Method Application**

#### 189 **3.1 Dataset**

190 Our study examines 8 events with magnitude  $M \geq 5.0$  using the waveform data  
191 retrieved from the Center for Engineering Strong Motion Data (CESMD, see Data and  
192 Resources) . We run playback of seismic data from each earthquake event through FinDer  
193 algorithm in a simulated real-time mode to generate the temporal point source or finite  
194 source solutions including source locations (centroid or line-source), rupture-to-site  
195 distance and magnitude, which are converted from the rupture length-magnitude scaling  
196 relationship (Wells & Coppersmith 1994). Once the source solution become available, the  
197 source solution is used in concert with the selected GMPE (Boore et al. 2008; Atkinson  
198 and Boore 2011) to provide predictions of the expected ground shaking including PGA  
199 and PGV (Peak Ground Velocity). We then apply the ground motion and intensity  
200 conversion equation (GMICE) of Wald et al. (1999) to calculate the MMI intensity  
201 envelope for each individual site. For the observed intensity, we calculate the peak ground  
202 motions by determining the maximum value of amplitudes on the two horizontal  
203 components of waveform data. The observed ground motion amplitudes are also  
204 converted into ground motion instrumental intensity envelopes in the same manner as the  
205 predicted ground motions.

206 **(Fig.1, about here)**

#### 207 **3.2 FinDer Source Characterization**

208 The detailed temporal evolving of source solutions in Fig. 1b, Fig. 2 and Fig. A1-2 in  
209 supplementary information for three main events, and the final optimum line source  
210 summarized in Fig. 1a and Table 1 for all the eight events show the algorithm performance  
211 neglecting the data latency.

212 For the  $M_w 7.1$  mainshock, after 3.5 s from the event origin, FinDer generates the  
213 initial source solution with estimated magnitude as  $M 3.5$  using the empirical rupture

214 length-magnitude scaling relationship in equation (3). At 7.5 s from origin time, which  
215 approximately corresponds to the trigger time at which the initial magnitude solution was  
216 released by ShakeAlert (6.9 s), FinDer estimates the magnitude as M5.5 (Fig. 2b). The  
217 preferred line source model shows that the rupture orients towards NW bilaterally 12 s  
218 after origin time due to clustered stations distributed within the northwestern region of  
219 epicenter (Figs. 2c-e). FinDer's source solution stabilizes 23.5 s after origin time with a  
220 rupture propagates dominately toward SE along fault of L = 54 km (M6.9) with rupture  
221 orientation of  $\Theta = 136^\circ$ (Fig. 2f). This result agrees well with 22 s of rupture duration and  
222 54 km-long surface rupture suggested by filed survey and the waveform inversion results  
223 (Stewart et al. 2019; Ross et al. 2019; Wang et al. 2020b).

224 The ShakeAlert EEW system issued a first alert message for the  $M_w$ 6.4 event with an  
225 initial magnitude of M5.7 estimated by EPIC at 6.9 s from earthquake occurrence, and  
226 FinDer generate a first magnitude estimate of M5.5 0.6 s later (Chung et al. 2020). These  
227 observations coincide with the the results derived from the retrospective results of FinDer  
228 alone in Fig. 2c. The final FinDer line source model is achieved 31.7 s after the earthquake  
229 occurrence with a strike of  $150^\circ$ and a rupture length of 21 km owing to the data latency  
230 (Chung et al. 2020). Although the orientation of the final FinDer line source differs by  
231  $17^\circ$ compared to the W-phase moment tensor solutions, the final rupture length is  
232 estimated as 29 km (M6.5), which is overestimated compared to waveform inversion  
233 results of Wang et al. (2020b; L = 20 km), but the estimated magnitude fits well with the  
234 moment magnitude ( $M_w$ 6.4; USGS 2019). The final optimum source solution of FinDer  
235 favors a NW-SE plane with a rupture duration of 13.5s (Fig. A1f). Although the evidence  
236 revealed by filed survey and some geodetic measurement suggested the foreshock didn't  
237 rupture along the northwest-striking segments on surface (Stewart et al. 2019; DuRoss et  
238 al. 2020; Hudnut et al. 2019; Milliner and Donnellan 2020). Most of seismic and geodetic  
239 studies, and aftershock distribution corroborated that the  $M_w$ 6.4 event involves two  
240 orthogonal fault strands with moderate slip on the NW oriented fault segments in depth,  
241 which played important role in initiating the mainshock (Ross et al. 2019; Chen et al. 2019;  
242 Feng et al. 2020; Wang et al. 2020a; Wang et al. 2020b).

243 For the foreshock  $M_w$ 5.4 event, The first solution comes in 3.5 s after time origin with  
244 magnitude estimated as M3.8 (Fig. A2a), the final update to the stable line source is  
245 determined within 13 s after origin time and has a length of L = 6.0 km (M5.5) and azimuth  
246 of  $\Theta = 117^\circ + 180^\circ$  due to the symmetry of the line source model (Fig. A2f). For the  
247  $M_w$ 5.4 event after the mainshock, the final solution of line source is estimated as  $\Theta =$   
248  $145^\circ + 180^\circ$ , which is in good agreement with the second nodal plane of the USGS  
249 Moment Tensor solution of  $339^\circ$ , but the rupture length is underestimated as 1.3 km  
250 (corresponding to M4.5) because of the sparse station coverage in the near source region  
251 with interstation distance of 30.1 km and sparseness of  $45^\circ$ and algorithm configuration.  
252 The inerstation distance is defined as the average distance between the epicenter to the

253 three closest stations (Li et al., 2021). The degree of sparseness is calculated according to  
254 the arithmetic sum of angular sectors with every  $15^\circ$  azimuthal range having zero stations  
255 in this article (Convertito et al. 2012). Furthermore, FinDer requires at least two stations  
256 exceed the predefined ground motion amplitude ( $2 \text{ cm/s}^2$ ) in this issue. Other four events  
257 occurred within region with high degree of sparseness of  $\geq 45^\circ$ , which eventually results in  
258 magnitude underestimation and great location errors (Table 1). Therefore, we only include  
259 three main events into the following alert performance analysis.

260 (Fig. 2, about here)

### 261 3.3 The Simulated Real Time Alert Performance

262 When the temporal results of line source model determined by FinDer updates in  
263 every 0.5 s, we can successively calculate the estimated magnitude and fault distance as  
264 more seismic data becomes available over time, FinDer continues to revise its source  
265 solution and derives from those the ground motion amplitudes according to the GMPE of  
266 Boore and Atkinson (2008) and Atkinson and Boore (2011). The resulting predicted  
267 amplitudes will subsequently be converted to MMI intensity envelope after the GMICE of  
268 Wald et al. (1999). As illustrated in Fig. 2 for mainshock, FinDer enables determine the  
269 potential affected shaking zone characterized by respective contour lines in real time until  
270 fault rupture terminates when applying the alert criterion of  $\text{MMI}_{\text{alert}} = 3.5$ . For the  
271 observed intensity, we combine the peak strong motion amplitudes (PGA, PGV) to  
272 compute instrumental intensity envelopes for each individual site in the same manner as  
273 the predictions. Then the temporal evolution of the observed and predicted intensity  
274 envelope updates as the FinDer magnitude and orientation of line source changes. When  
275 applying the lower alert threshold and higher damage threshold, a potential expected  
276 consequence is to yield better classification as suggested by previous tentative and  
277 observational studies (Minson et al. 2019; Ruhl et al. 2019; Meier et al. 2020; Chung et al.  
278 2020). To evaluate the influence of alert criterion exerting on the classification  
279 performance during the Ridgecrest earthquake sequence, we provide six choices of alert  
280 criterion to explore in which circumstance FinDer algorithm can achieve the best alert  
281 performance including classification.

282 Applying the alert criterion of  $\text{MMI}_{\text{alert}} = \text{MMI}_{\text{tw}} = 3.5$ , Fig. 3 presents the available  
283 warning time for sites with different intensities and hypocentral distances for three main  
284 events. We observe that more distant sites from the epicenter with lower intensities usually  
285 have higher potential of receiving long warning times (Figs. 3-4). Illustrating the  $M_w 5.4$   
286 event for example, A near-epicentral site CI.TOW2 with hypocentral distance of 19.1km  
287 would have the difficult in being timely alerted in real EEW system with only 1 s of  
288 actionable time. A site (CI.CCC) ( 35.4 km) records the maximum instrumental intensity  
289 (MMI 8.9) during the mainshock located within the forward directivity region, timely alert  
290 is still possible, the observed ground motion intensity is still low (MMI 1.0) when it gets

291 alert, the predicted intensity has increased up to MMI 5.2 within the available warning  
292 time (3.5 s from the first alert), and peak shaking arrives until 18 s after the first alert (Fig.  
293 3c). A key feature of earthquake arises from the fact that earthquake initiates as a point, the  
294 rupture evolves through time to propagate over the fault. There exists potential regions  
295 that are distant from the epicenter but close to the fault plane, which allows sufficient  
296 warning times to alert updates only in the rare cases of very large events such as  
297 Ridgecrest,  $M_w7.1$  event. Additionally, as illustrated by the gray shaded region in Figure  
298 3c , higher potential for long warning times are expected for sites which locate farther  
299 away from the epicenter.

300 **(Fig. 3, about here)**

301 For an alert criterion of  $MMI_{alert} 3.5$ , Fig. 4 shows the warning time map for three  
302 main events. Overall, It coincides with the general expectation that warning time increases  
303 with hypocentral distance. As for the  $M_w7.1$  event in Fig. 4a, only one site with above  
304 threshold amplitude misses the chance to be timely alerted because the actual strong  
305 shaking has arrived before FinDer's trigger criterion is met in this issue (at least 2 sites  
306 surpass the ground motion level of  $2\text{ cm/s}^2$  for event declaration). The trigger criterion is  
307 more conservative in ShakeAlert (4 sites for trigger, Böse et al. 2021). When actual ground  
308 motions reach  $MMI_{tw} = 3.5$ , an alert will not be regarded as to be useful because the  
309 shaking is already too strong to initiate risk mitigation actions. Large fractions of false  
310 alerts distributes in the Los Angeles, Oxnard and Banning regions. Most of false alerts  
311 including either the FP or FN cases occur near the contour line of alert threshold (Fig. 4a).  
312 It is important to mention that uncertainties arise from source characterization, GMPE and  
313 GMICE, and site effect will impose great constraint on the accuracy of ground motion  
314 estimates. For the  $M_w6.4$  event, large factions of sites has been classified as false negative  
315 cases because of underestimated ground motions in the Oxnard and Los Angeles regions  
316 (Fig. 4b). For the  $M_w5.4$  event, two false negative cases occurs at the near-epicentral sites,  
317 all sites with below threshold amplitude locate outside but near the delimited area of  
318 observed MMI intensity of 3.5 (Fig. 4c). Indeed, there exists late-alert zone near the source  
319 where no warning time is available prior to the arrival of strong shaking because it  
320 consumes times for source-based EEW system including FinDer for event detection  
321 before generating alerts. As a general result, useful alerts with potential longer warning  
322 time are less likely for small earthquakes with contrast to large magnitude events (Fig. 4).

323 **(Fig. 4, about here)**

324 Fig. 5 illustrates the detailed classification performance using three choices of alert  
325 criteria for the total earthquake sequence. Full circles show predicted intensities made  
326 timely before the observed intensities exceed the damage threshold. Empty circles are  
327 predicted intensities without taking warning time into account. The selected sites are  
328 classified as four categories: TP (True Positives), TN (True Negatives), FP (False

329 Positives), FN (False Negatives). A visual inspection of the classification shows that the  
330 deviation between observed and timely predicted ground motion intensities falls within  
331 the range of  $\pm 1$  MMI unit. But there appears that the discrepancy especially for high  
332 intensities is relatively large, even the extreme circumstance in which some of these sites  
333 still have none of prediction been made with  $MMI_{pred} = 0$  owing to impulsive ground  
334 motion has arrived before FinDer detects the event at that point of time. These cases imply  
335 that high intensities are generally the most difficult cases to be warned in advance.

336 Concerning the total earthquake sequence, over 74% of the sites are correctly  
337 classified as true alerts, and almost 5% of sites are underestimated as  $MMI < 3.5$  but over  
338 20% are overestimated as  $MMI \geq 3.5$  when applying the alert criterion of  $MMI_{alert} 3.5$ . As  
339 a general result, much fractions of sites would have the chance to be alerted by applying  
340 lower alert threshold accompanying a substantial reduction of false alerts , FinDer rates  
341 over 91%, 74% and 94% true alerts for alert threshold of  $MMI_{alert} 2.5, 3.5$  and 4.5,  
342 respectively (Fig. 5 and Figs. A3-4 in supplementary information). Applying lower alert  
343 threshold of  $MMI_{alert} 2.5$ , over 94% of alerts would have been correctly assigned among  
344 all the released alerts, only almost 5% alerts are cases that should have been alerted but  
345 eventually failed to do. The corresponding fractions are 68% and 50% for  $MMI_{alert} 4.5$ .  
346 Overall, the classification is expected to perform better for applying lower alert threshold  
347 for both the three respective events and the total earthquake sequence (Fig. A4). Note that  
348 false alerts almost come from observed ground motion intensities near the alert threshold  
349 (Fig. 5).

350 As the fiftieth percentile curves show, overall, FinDer predicts well the low  
351 intensities (1.5-4.5), but even if applying lower alert threshold and higher damage  
352 threshold, predictions made within available warning time obviously underestimate the  
353 high intensities ( $MMI > 4.5$ ) if the prediction error tolerance level is set to 0.5 MMI unit  
354 (Fig. 5 and Figs. A3-4). Indeed, FinDer just captures the current available information  
355 from observed ground motion to associate with the source solution, but FinDer attempts  
356 not to predict the future evolving rupture, which would have upgraded into large scales  
357 through time after observed ground motion has exceeded the predefined damage threshold.  
358 Therefore, it is of comparatively challenging that we predicts high intensities accurately  
359 within invariable few seconds of warning time.

360 **(Fig. 5, about here)**

361 The usefulness of EEW algorithm including FinDer can be assessed by introducing  
362 the cost reduction metric from end-user-orientated perspective (Minson et al. 2019; Meier  
363 et al. 2020a; equation(4)). The cost reduction metrics is defined involving two aspects: (1)  
364 the cost ratio  $r$ , which is a user-dependent parameter associated with end users' tolerance  
365 level for false alerts, only when earthquake damage losses outweigh action costs with  
366 distinguishable high cost savings are regarded as meaningful for motivating end user to

367 initiate risk mitigation actions (Cochran & Husker. 2019; Meier et al. 2020a). (2) the  
 368 respective percentages of three categories of alerts excludes true negatives due to its  
 369 characteristic of susceptible to be influenced by cutoff distance used for the record  
 370 selection (Meier et al. 2020a).  $r = C_{\text{damage}} / C_{\text{action}}$ ,  $C_{\text{damage}}$  is the cost of the damage,  
 371  $C_{\text{action}}$  is the cost of taking action to prevent the damage. The CR metric can be adapted in  
 372 concert with the classification performances stated above (Minson et al. 2019).  
 373  $m = N_{\text{FN}} / N_{\text{TP}}$ ,  $f = N_{\text{FP}} / N_{\text{TP}}$ .  $m$ ,  $f$  represents the missed alert rate and the false alert rate,  
 374 respectively.

$$375 \quad \text{CR} = \frac{1 - \frac{f+1}{m+1}}{r} \quad (4)$$

376 During the Ridgecrest earthquake sequence, FinDer yields more false alerts  
 377 especially FN cases with higher alert threshold (Fig. 6a). We can conclude that the alert  
 378 threshold will obviously affect the classification and thus CR performance. Meanwhile,  
 379 we obtain negligible differences over classification by increasing the damage threshold,  
 380 thus FinDer can be expected to result in indistinguishable higher cost reduction by  
 381 applying the higher damage threshold inferred from classification statistics (Fig. 6b).  
 382 Therefore we calculate CR values across a wide range of cost ratios using three choices of  
 383 alert criteria. The highest CR value are found for applying the alert criterion of  $\text{MMI}_{\text{alert}}$   
 384 2.5 (85%,  $r = 10$ ), the corresponding CR values are 51% and 43% for alert threshold of 3.5  
 385 and 4.5, respectively. It is worth noting that we include only three events into our analysis,  
 386 thus these statistics are interpreted as the cost reduction performance just for the  
 387 Ridgecrest earthquake sequence with lack of high intensities within near source region.  
 388 The observed discrepancies in terms of cost reduction between choices of alerting criteria  
 389 highlight that end user with high cost ratio can receive higher cost savings if they are  
 390 alerted for low shaking level, which is consistent with the conclusion drawn from previous  
 391 observations (Minson et al. 2019; Ruhl et al. 2019; Meier et al. 2020a).

392 **(Fig. 6, about here)**

393 Figs. 7-8 summarize the alert performance taking into account the warning time for  
 394 three main events in the total sequence. Figs. 7a-c illustrate the empirical cumulative  
 395 distribution as a function of warning times by disaggregating the sites into different bins of  
 396  $\text{MMI}_{\text{obs}}$  (2.5:1:9.5) when we apply three alert criteria of  $\text{MMI}_{\text{alert}}$  2.5, 3.5, and 4.5. We  
 397 observe that useful alerts are more possible for sites with low intensities with contrast to  
 398 high intensity sites. In general, the empirical cumulative distribution of warning times

399 exhibits a inverse correlation with observed ground motion intensities for most of intensity  
400 bins, but high intensity bin (8.5:9.5) achieves longer median warning time due to only one  
401 site CI.CCC included into the analysis, and longer warning time favors the sites which  
402 locate near the fault rupture but far away from the epicenter.

403 Applying a broad range of alerting criteria, the median warning time can be fairly  
404 long ( $\sim 25$  s) for sites with light to moderate intensities (MMI 4.5-5.5) regarding the  
405  $M_w 7.1$  and  $M_w 6.4$  events, but for the  $M_w 5.4$  event, light to moderate intensities often  
406 occur within the near source region with median warning time of 3 s or less (Figs. A5-6  
407 supplementary information). For the moderate and strong intensities (MMI 5.5-6.5), over  
408 half of sites can be alerted with warning time of 16 s for the  $M_w 7.1$  event, the fraction is 3.5  
409 s for  $M_w 6.4$  event (Figs. A5-6). These observations showcase that with respect to FinDer,  
410 there is higher potential for long warning time for large magnitude events such as  $M_w 7.1$   
411 event than there is for small to moderate events.

412 Concerning for the total earthquake sequence (Figs. 7a-c), for weak to light intensities  
413 (MMI 3.5-4.5), 50% can be alerted with warning time of almost 40s and 20s for  $MMI_{alert}$   
414 2.5 and 3.5, respectively. Sites that experiencing light to moderate shaking (MMI 4.5- 5.5,  
415 green curves in Fig. 7) are alerted for  $MMI_{alert}$  2.5 and 3.5, 50% would have received a  
416 warning time of 20 s, the fraction is less than 25% for  $MMI_{alert}$  4.5. For the moderate to  
417 strong intensities (MMI 5.5-6.5), 55% can be correctly alerted with warning time of 10 s  
418 for  $MMI_{alert}$  2.5 and  $MMI_{alert}$  3.5, the fraction is 18% for  $MMI_{alert}$  4.5. For moderate and  
419 strong intensities, 45% can be correctly alerted with warning time of 10 s for  $MMI_{alert}$  2.5  
420 and  $MMI_{alert}$  3.5, only 18% would have received warning times of 10 s for  $MMI_{alert}$  4.5. If  
421 warning times are computed with the alert threshold varying from 2.5 to 4.5 and the  
422 damage threshold is set to  $MMI_{tw}$  4.5 (Figs. 8a-c). For light to moderate intensity sites  
423 distributed within about 240 km of epicenter, almost 50% would have received warning  
424 times of more than 35 s for  $MMI_{alert}$  2.5 and  $MMI_{alert}$  3.5, only 25% with warning time of  
425 16 s for  $MMI_{alert}$  4.5 due to over half of sites has failed to be alerted. For the moderate and  
426 strong intensities within 160 km of epicenter, 55% can be correctly alerted with warning  
427 time of 10 s for  $MMI_{alert}$  2.5 and  $MMI_{alert}$  3.5, the fraction is 18% for  $MMI_{alert}$  4.5. In  
428 contrast, strong to violent shaking (MMI 6.5-9.5) often occurs on near-epicentral sites  
429 within about 40 km of epicenter and warning times longer than 5 s are rarely possible even  
430 for  $MMI_{alert}$  2.5. We can conclude from these observations that useful alerts are more  
431 likely for lower alert threshold, and sites with high intensities are the most difficult cases  
432 to be correctly alerted in real EEW systems if including data latency, indeed, FinDer are  
433 therefore most relevant for more distant target sites.

434 As stated above, warning time ranges from few to tens of seconds, which varies with  
435 the observed intensity and the different alert criterion. Negative warning times distributed  
436 within distances smaller than 20 km, where warning time is invariably on the order of few

437 seconds for high intensities, sites within region of 40 to 80 km from epicenter can receive  
438 warning time of 7.5 - 19 s for the median, and warning times are over 20 s on average for  
439 distance larger than 100 km (Figs. 7,8 a'-c'). Furthermore, much fractions of sites would  
440 have been alerted if applying lower alert threshold, and it coincides with the general  
441 expectation that sites from most of distance bins can achieve increased warning time if  
442 applying lower alert threshold (Figs. 8a'-c').

443 Although previous observations show that the damage threshold will not impose  
444 distinguishable influence on classification performance, but longer warning times are  
445 achieved by applying higher damage threshold (Fig. 8). For instance, 18% sites with  
446 moderate to strong shaking level can be alerted with warning time of 10 s for  $MMI_{alert} = 4.5$   
447 (Fig. 8c), the fraction is 55% for lower alert threshold (Figs. 8a-b).

448 **(Fig. 7, about here)**

449 **(Fig. 8, about here)**

450 It is worthy noting that the threshold based alert scheme brings in non-negligible  
451 truncation effect on the warning time for the intensity bin (3.5-4.5) near the alert threshold,  
452 only half of sites can be alerted with warning time of 10 s for  $MMI_{alert} = 3.5$ , but the  
453 fraction amounts to 98% if applying the lower alert threshold of  $MMI_{alert} = 2.5$ . Indeed,  
454 this can be ascribed to the decreased number of correctly alerted sites due to classification  
455 errors near the alert threshold. This is inevitable because GMPE usually predicts the  
456 median ground motion regardless of uncertainties introduced by forward directivity, path  
457 and site amplification effect (Irevolino et al. 2009; Minson et al. 2018). Meier (2020a)  
458 suggested that if certain classification tolerance is allowed, fractions of false alerts can  
459 eventually turn out to be useful to be successfully alerted.

### 460 **3.4 Accuracy of Ground Motion Predictions**

461 Figs. 9a-d plots the ground motion prediction errors as a function of warning time for  
462 three respective events and the total earthquake sequence. Warning time here is defined as  
463 the time relative to the time when the observed ground motion exceeds the damage  
464 threshold or theoretical S-wave arrival for sites with below-threshold ground motion  
465 (Meier et al. 2017b; Böse et al. 2018). We observe that the residual between observed and  
466 predicted ground motion are nearly stable around zero on average as shown by the median  
467 prediction errors curves, although the scatter is quite large (Figs. 9a-d). Such scatter will  
468 be translated into false alerts in a real EEW system. FinDer underestimates the ground  
469 motion intensities within a range of 0.3 units for three respective events. Concerning the  
470 total earthquake sequence, when sites still have available 5 s of warning time,  
471 overpredicted ground motions are typically off by almost 0.7 MMI unit (as illustrated by  
472 95th percentile of error distribution curve), and underpredicted ground motions within the

473 range of 1 unit as shown by the 5<sup>th</sup> percentile curve. The scatter around the median is  
474 within the range of -0.7 ~0.9 MMI units with decreasing warning time, this can explain  
475 fractions of false alerts(Fig. 9d). The prediction errors disaggregated according to different  
476 intensity bins (1.5:1:8.5) in Figs. 9e-f illustrate that in general, FinDer predicts well the  
477 weak to moderate intensities (MMI1.5-5.5) on average, instead, FinDer underestimates  
478 sites with moderate to severe intensities (MMI 5.5-8.5). For sites with moderate to very  
479 strong ground motion intensities (MMI 5.5-6.5), the predictions underestimate the  
480 observed ground motions by 0.9-1.15 MMI unit within available warning time for the  
481 median, the fractions are 1.4 unit for sites with moderate to very strong ground motion  
482 intensities (MMI 6.5-7.5) even if applying the lower alert threshold and higher damage  
483 threshold as illustrated by Figs 9e-f .

484 These observations further confirm that despite accurate prediction of high ground  
485 motion intensities within the near source region constitutes the primary concern for EEW  
486 systems, majorities of sites with high intensities are rarely possible to be accurately  
487 predicted ahead of time albeit correctly alerted owing to high intensities often occur at  
488 near-epicentral sites with potential warning times invariably on the order of few seconds.

489 (Fig. 9, about here)

### 490 3.5 Discussions and Future Remarks

491 FinDer detects all the events within 6.5 s from earthquake occurrence leveraged from  
492 relatively dense station density in Southern California. But currently, the ANSS seismic  
493 networks are not dense enough to cover all areas especially where faults have not been  
494 mapped (Kohler et al. 2018). Thus, sparse instrumentation and inappropriate geometry of  
495 seismic network, and processing and algorithm delays will inevitably lead to  
496 late-alert-zone for any source-based EEW algorithm (Behr et al. 2016). This roughly  
497 corresponds to a region with radius of over 20 km assuming an approximate propagation  
498 speed of 3.75 km/s in Southern California (Mori et al., 1996; Wurman et al. 2007). With  
499 regard to FinDer, the dimension of late-alert-zone actually depends on the network  
500 geometry thus the relevant algorithm trigger threshold predefined as the amplitude  
501 exceedance level surpassed by the minimal number of stations (Li et al. 2021). But  
502 warning times would hardly change for decreased station spacing beyond certain limits  
503 due to the processing and algorithms delays also contributing to the data latency (Kuyuk et  
504 al. 2013; Behr et al. 2015). During the 2019, Ridgecrest earthquake sequence, poor station  
505 density and azimuthal coverage or high degree of sparseness within the near source region  
506 are responsible for great location error and magnitude underestimation for events of  $M \leq$   
507 5.4 (Table 1). Indeed, latencies arise from alert transmission and delivery will also  
508 eventually result in failure for alerts with limited warning times in operational EEW  
509 systems. Furthermore, many involving procedure can result in false alerts such as

510 inaccurate source characterization, cumulative uncertainties propagated through selected  
511 GMPE, GMICE, and site amplification, or algorithm's intrinsic incapability of accurately  
512 predicting high ground motion intensities. Overall, during 2019, Ridgecrest earthquake  
513 sequence, FinDer predicts well the ground motion intensities. The final FinDer magnitude  
514 estimate for the three main events coincides well with the reference event catalog with a  
515 difference of  $\pm 0.2$  magnitude units, thus the predictions are not biased with respect to the  
516 observed ground motions on average. It worth noting that the rupture length estimate of 54  
517 km during the mainshock agrees well with the surface rupture and waveform inversion  
518 results, the final magnitude underestimation can be ascribed to uncertainty introduced by  
519 the empirical rupture length to magnitude scaling relationships. Indeed, dynamic  
520 characteristics of rupture process mostly correlates with high frequency aspects of seismic  
521 measurements but not the moment release (Baltay et al. 2013; Picozzi, et al. 2017).

522 Compared to point-source algorithms, FinDer usually delays to respond in source  
523 characterization but capable of offering more reliable source solution especially for large  
524 magnitude events. For example, EPIC measures initial portion of peak P wave amplitude  
525 ( $P_d$ ) to predict the eventual size of magnitude, but during the Ridgecrest earthquake  
526 sequence, the discrepancy with respect to the  $P_d$  measurement between the  $M_w7.1$  and  
527  $M_w6.4$  events is indistinguishable at least within the early 4 s window of seismic data  
528 (Chung et al. 2020). Previous studies also indicate that the saturation of P wave  
529 displacement will likely to occur within near source region during large magnitude events  
530 (Olson & Allen 2005; Wurman et al. 2007; Trugman et al. 2019). As a result, the  
531 information revealed by first few seconds of P wave can't predict well or weakly predicts  
532 the realistic evolving rupture before the source time function is complete or mostly  
533 reached (Meier et al. 2016; Melgar et al. 2017; Meier et al. 2020b). It appears that  
534 interpretation of the extended fault rupture in real time can add significant value to the  
535 EEW warnings (Böse et al. 2018; Ruhl et al. 2019). Most notably, ShakeAlert alerts  
536 contributed by EPIC and FinDer must be in accordance together with a upper limit of 30 s  
537 for the origin time and 100 km for the location error (McGuire et al. 2021a). Meanwhile,  
538 ShakeAlert puts higher weight on EPIC than FinDer regarding the magnitude estimate.  
539 Although these strategies, to great extent help to reduce false triggers due to sparse  
540 instrumentation or solve for difficulty in dealing with intense aftershock sequence, but  
541 also drag down the FinDer' unsaturated magnitude estimation (Chung et al. 2020). As  
542 always, there is a trade-off or reconcile of timeliness versus reliability between algorithms  
543 in ShakeAlert. Providing alerts with fast speed leads to a loss of accuracy due to the  
544 limited information available, whereas, a higher degree of reliability must be at cost of loss  
545 of warning time.

546 How timely can FinDer generate useful alerts prior to the onset of strong ground  
547 shaking, and with what accuracy to predict ground motion intensities? How will this  
548 timeliness and accuracy be translated into alerts for end-user applications with threshold

549 based alert scheme? A key component underpinning the utilities of EEW system including  
550 FinDer in hazard reduction is to provide a quantitative understanding how much warning  
551 time will be available and how that will vary with hypocentral distance, and observed  
552 intensity under different alert criteria. In this article, we classify the alerts into four  
553 categories to quantify the alert performance in simulated real time environment by  
554 introducing the MMI-threshold alert evaluation metric. Concerning the 2019, Ridgecrest  
555 earthquake sequence if not taking the data latency into consideration, FinDer generates  
556 large fractions of useful alerts including the most difficult cases with high ground motion  
557 intensities. FinDer rates over 74% of true alerts across a wide range of alert criterion. We  
558 find that FinDer achieves better classification with higher cost savings using lower alert  
559 threshold during the Ridgecrest earthquake sequence due to the decreased missed and  
560 false alert rate. Furthermore, FinDer obviously underestimates the high intensities  
561 attributed to the intrinsic difficulty of predicting accurately the high intensity sites located  
562 within the near source region (Meier et al., 2020a; Wald et al., 2020). Some work has  
563 investigated on the reliability of EEW algorithms for warning high intensities in case of  
564 large earthquakes, but this has so far been limited to the simulated events, or under certain  
565 specific tectonic regime (e.g. subduction zone) (Meier et al. 2020a; McGuire et al. 2021a).  
566 In addition, the actual peak shaking often arrives with either destructive S wave or surface  
567 wave, allowing somewhat additional actionable time (Parolai 2015; Picozzi et al. 2015;  
568 McGuire et al. 2021a).

569 Note that FinDer just captures the occurring rupture conditioned on the current state  
570 of knowledge at a given instant, but attempts not to predict beyond the future affected zone  
571 where observed ground motion amplitudes are actually accumulating. Currently, Böse et  
572 al. (2021) proposed upgraded version of FinDer called FinDerS(+) to assimilate  
573 information from wide spectrum source data thoroughly to predict the future size of  
574 evolving rupture, FinDerS(+) further develops capability of taking into account the  
575 structural maturity of the overall fault in a systematic way, which governs the slip  
576 heterogeneity thus the dynamic stress drop release (Liu et al. 2005; Manighetti et al. 2007).  
577 Previous observations was spontaneous in the sense that the youthful or immature fault  
578 exhibiting highly segmentation or orthogonal cross-faulting geometry (e.g. 2016,  $M_w$ 6.2  
579 Amatrice earthquake, Italy; 2019, Ridgecrest earthquake sequence) unfavorably oriented  
580 for rupture (Manighetti et al. 2005; Gallovc̃ et al. 2019).

581 Indeed, An integral EEW system consists of exhaustive interconnected aspects  
582 including data sources, algorithms, event associator, and alert generation and delivery  
583 (Given et al. 2014; Kohler et al. 2018). EEW system should be given priority to maximum  
584 reliability to reduce false triggers with high detection success, many promising approach  
585 (e.g. Machine Learning) have been proposed to tackle with intense aftershocks,  
586 multi-events and noise data to achieve more robust event discrimination (Böse et al. 2009;  
587 Liu & Yamada 2014; Meier et al. 2019). Currently, an effective operational EEW system

588 is also no longer restricted to single data source and algorithm. Geodetic measurements  
589 such as high-precision GNSS (Global Navigation Satellite Systems) data has also been  
590 included into EEW for unsaturated magnitude estimation (Allen and Ziv 2011; Minson et  
591 al. 2014; Grapenthin et al. 2014; Crowell et al. 2016; Kawamoto et al. 2017). In the future,  
592 Gravity strainmeters, low-cost sensors such as micro-elctro-mechanical system (MEMS)  
593 accelerometers, carried by various medias will greatly supplement the traditional EEW  
594 system to achieve spatially much denser networks (Juhel et al. 2018; Horiuchi et al. 2009;  
595 Cochran 2009; Fleming et al. 2009; Wu et al. 2013; Piccozi et al. 2014; Kong et al. 2016).  
596 Also combining algorithms with different mechanisms leveraged from various type of  
597 data available will provide more reliable source solutions thus ground motion predictions.  
598 For instance, threshold-based approach in Southern Italy version of EEW system  
599 integrates network-based PRESTo (PRobabilistic Evolutionary early warning SysTem)  
600 with On-site algorithm by incorporating evolutionary estimation of location, magnitude  
601 and potential damage zone (Zollo et al. 2010; Colombelli et al. 2012; Zollo et al. 2014).  
602 The Japan Meteorological Agency (JMA) plans the hybrid use of regional, on-site and  
603 ground motion based methodology such as PLUM to optimize the EEW performance  
604 (Kanamori 2005; Kamigaichi et al. 2009; Hoshiha and Aoki 2015; Kodera et al. 2016).  
605 Since 2018, the implementation of ShakeAlert combines two network-based algorithms  
606 including EPIC and FinDer to utilize the capability of source-based EEW approach to  
607 the maximum extent. ShakeAlert strikes a balance between the timeliness of alerts for  
608 near-source targets in small magnitude events and also the accuracy of alerts for realistic  
609 evolution of occurring rupture in case of large magnitude events. Additionally, ShakeAlert  
610 is also underway to incorporate geodetic EEW algorithms into the production system  
611 (Cochran et al. 2018; Given et al. 2018). Combination of ElarmS with geodetic algorithm  
612 (e.g., G-larmS, BEFORES) from geodetic and seismic measurements will achieve mutual  
613 advantages on achieving timeliness in event detection and also accuracy in magnitude  
614 estimation, in spite of the fact that realistic expectations from geodetic approaches in risk  
615 mitigation especially for high intensities under complex tectonic regimes deserves further  
616 investigation from technical perspectives (Ruhl et al. 2017; McGuire et al. 2021b).  
617 Meanwhile, some researchers has dedicated to develop evolutionary probabilistic decision  
618 framework to integrate source parameters thus ground motion predictions from various  
619 algorithms into unified and more reliable shaking forecast (e.g., Minson et al. 2017).  
620 Indeed, many promising algorithms aim to a particular class of magnitude events, but the  
621 main challenge remains in the consistent implementation for real-time characterization of  
622 the occurring rupture. But FinDer performs in an evolutionary manner to guarantee a  
623 consistent description of point source or occurring rupture to extend identifiable  
624 earthquake events to the entire range of magnitudes. Furthermore, any EEW system  
625 should be engineering to achieve the optimal warning functions with acceptably low data  
626 latency. During the Ridgecrest earthquake sequence, telemetry latencies including data  
627 packeting and limited bandwidth of station data-logger greatly constrained the source

628 characterization of FinDer (Chung et al. 2019; Stubailo et al. 2020), the retrospective  
629 study in this issue is conducted without accounting for the delays from field telemetry and  
630 alert delivery. To ensure reliable operation of the EEW algorithm including FinDer,  
631 appropriate telemetry infrastructure should be designed to minimize the data latency  
632 within a allowable low level through various delivery means including radio, internet, and  
633 smartphone applications (McGuire et al. 2021a). Whichever data sources, algorithms,  
634 telemetry infrastructure are adopted, reliable source solutions will be eventually translated  
635 into useful alerts and accurate ground motion predictions. Of primary concern is the  
636 accuracy of magnitude estimate and location in the early phase of EEW production system,  
637 but now more concerned for end users is the actual target of warning notification of  
638 impending strong shaking. Most existing EEW algorithms or systems adopt geotargeting  
639 strategy to combine the real-time estimates of earthquake magnitude and the potential  
640 shaking that will experience for particular end users with various demands (Zollo et al.  
641 2010; Doi et al. 2011; Colombelli et al. 2012; Given et al. 2018; Böse et al. 2018; McGuire  
642 et al. 2021a). The geotargeting approach makes it practical for the algorithm  
643 implementation to characterize the potential damage zone in real time. During the  
644 Ridgecrest earthquake sequence, we also observe that the alert threshold brings in  
645 truncation effect for the sites with near threshold amplitude because of the uncertainties  
646 stemmed from inaccurate source characterization, selected GMPE, GMICE, and local  
647 discrepancies, moreover, the propagation of these uncertainties and thus cumulative  
648 effects imposed on the resulting ground motion predictions further weaken the potential  
649 for correct decision-making on alert release (Iervolino 2011; Cremen et al. 2021).  
650 Therefore, criterion for alert release will be optimized for less false alerts with lower alert  
651 threshold according to theoretical studies and previous observations (Minson et al. 2019;  
652 Ruhl et al. 2019; Meier et al. 2020a; Chung et al. 2020; this issue). For instance, various  
653 alerting apps (including QuakeAlertUSA, City of Los Angeles and MyShake) in  
654 ShakeAlert system provide choices of lower alert criterion that, for events with magnitude  
655  $M \geq 4.5$ , alert all regions within the MMI 2.5 contour polygon (Chung et al. 2020;  
656 McGuire et al. 2021a). Additionally, accuracy evaluation in probabilistic manner will  
657 prevail on application for alert triggering to achieve well-informed decision making  
658 especially for multialgorithm EEW systems (Meier et al. 2017b; Minson et al. 2017;  
659 Cremen et al. 2021).

## 660 **4 Conclusions**

661 We have presented the application of the FinDer algorithm alone for the 2019,  
662 Ridgecrest earthquake sequence under maximally favorable conditions. Here we introduce  
663 end-user-orientated alert strategy to measure FinDer algorithm's reliability to generate  
664 useful alerts. We observe that, during the 2019, Ridgecrest earthquake sequence, network  
665 geometry including station spacing, especially degree of sparseness will exert great  
666 influence on the timeliness on event detection, accurate characterization of event source

667 thus resulting ground motion. Overall, for three main events, large fractions of sites would  
668 have been timely alerted with sufficient accuracy if appropriate algorithm configuration is  
669 deployed. Potential long warning time can be expected for sites far from epicenter  
670 especially in large magnitude events if the lower shaking level we adopt to alert for. As a  
671 general result, sites with high intensities are also a challenge for FinDer to generate  
672 reliable alerts prior to the onset of strong shaking. Furthermore, the amount of warning  
673 times for strong or worse shaking will be greatly discounted by practical difficulty of  
674 implementing this approach in the operational EEW environment. Regardless of these  
675 aforementioned constraints, FinDer nevertheless performs a consistent and predictive  
676 modeling approach tailored to entire range of magnitude events and thus to mitigate large  
677 percentages of preventable seismic hazards for early warning purpose in the future.

## 678 **5 Data and resources**

679 The observed acceleration data was retrieved via the CESMD database (Center for  
680 Engineering Strong Motion Data), (last accessed April 26, 2021). Basic event source  
681 information and focal mechanisms are obtained from the US Geological Survey  
682 (<http://earthquake.usgs.gov/earthquakes/>, last accessed April 28, 2021). The quaternary  
683 faults in Fig.1 are available from Quaternary Fault & Fold Database  
684 (<http://Qfaults.cr.usgs.gov/> , last accessed September 26, 2018 ).

685

686 Supplement information contains Figs. A1-2 with temporal results of finite source  
687 solution for two main evens including  $M_w6.4$  and  $M_w5.4$  earthquake, Figs. A3-4  
688 comparable to Fig. 5 in the main text about the detail classification performance for three  
689 main events and the total earthquake sequence, and also Figs. A5-6 corresponding to Fig.  
690 7-8 in the main text for empirical cumulative distribution of warning times for three  
691 respective events across a wide range of alert criteria.

692 **Acknowledgements** The waveform data for this issue are made freely available by the  
693 CESMD. Figures were made using Generic Mapping Tools (GMT) software version 5.4.2  
694 (<http://gmt-china.org/download/>, last accessed July 2020). And the analysis are made  
695 using Matlab software version R2021 64-bit (<http://it.mathworks.com/>, last accessed  
696 August 28, 2021).

697

## 698 **Compliance with ethical standards**

699 **Conflict of Interest** The authors declare that the research was conducted in the absence of  
700 any commercial or financial relationships that could be construed as a potential conflict of

701 interest.

## 702 **References**

703 Allen R M, and A Ziv (2011). Application of real-time GPS to earthquake early warning.  
704 Geophys Res Lett 38, L16310, doi: 10.1029/2011GL047947.

705 Atkinson G M, and D M Boore (2011). Modifications to existing ground-motion  
706 prediction equations in light of new data. Bull Seismol Soc Am 101, no. 3, 1121-1135.

707 Barnhart W D, Hayes G P, & Gold R D. (2019). The July 2019 Ridgecrest, California,  
708 earthquake sequence: Kinematics of slip and stressing in cross-fault ruptures. Geophys  
709 Res Lett 46, 11,859-11,867. <http://doi.org/10.1029/2019GL084741>

710 Baltay A, T Hanks, and G Beroza (2013). Stable stress-drop measurements and their  
711 variability: Implications for ground-motion predictions. Bull Seismol Soc Am 103,  
712 211-222.

713 Behr Y, J F Clinton, P Kästli, C Cauzzi, R Racine, and M -A Meier (2015). Anatomy of an  
714 Earthquake Early Warning (EEW) alert: predicting time delays for an end-to-end EEW  
715 system. Seismol Res Lett 86(3), 830-840, doi: 10.1785/0220140179.

716 Behr Y, Clinton J, Cauzzi C et al (2016) The virtual seismologist in SeisComp3: a new  
717 implementation strategy for earthquake early warning algorithms. Seismol Res Lett  
718 87(2A): 363-373. doi:10.1785/0220150235.

719 Bindi D, T Boxberger, S Orunbaev, M Pilz, J Stankiewicz, M Pittore, I Iervolino, E  
720 Ellguth, and S Parolai (2015). On-site early-warning system for Bishkek (Kyrgyzstan),  
721 Ann Geophys 58, S0112, doi: 10.4401/ag-6664.

722 Boore D M, and G M Atkinson (2008). Ground motion prediction equations for the  
723 average horizontal component of PGA, PGV, and 5%-damped PSA at spectral periods  
724 between 0.01 s and 10.0 s. Earthquake Spectra 24, no.1, 99-138.

725 Böse M, Hauksson E, Solanki K, Kanamori H, Wu Y -M, and Heaton T H. 2009. A new  
726 trigger criterion for improved real-time performance of On-site earthquake early warning  
727 in Southern California. Bull Seism Soc Am 99, 2-A, pp. 897-905, doi:  
728 10.1785/0120080034.

729 Böse M, Heaton T, Hauksson E. (2012). Rapid estimation of earthquake source and  
730 ground motion parameters for earthquake early warning using data from single  
731 three-component broad or strong motion sensor. Bull seism Soc Am 102 (2): 738-750.

732 Böse M, Fekizardo C, Heaton T H (2015). Finite-Fault Rupture Detector (FinDer) : Going  
733 real-time in Californian ShakeAlert warning system. Seismol Res Lett 86 (6): 1692-1704.

734 Böse M, Smith D E, Felizardo C, Meier M A, Heaton T H, Clinton J F (2018). FinDer v.2 :  
735 improved real-time ground motion predictions for M2-9 with seismic finite-source  
736 characterization. *Geophys J Int* 212 (1) : 725-742.

737 Böse M, Hutchison A A, Manighetti I, Li J, Massin Fé, and Clinton J F (2021). FinDerS(+):  
738 Real-time earthquake slip profiles and magnitudes estimated from backprojected  
739 displacement with consideration of fault source maturity gradient. *Front Earth Sci* 9:  
740 685879. doi: 10.3389/feart.2021.685879

741 Bracale M, Colombelli S, Elia L, Karakostas V, and Zollo A. (2021). Design,  
742 implementation and testing of a Network-based Earthquake Early Warning System in  
743 Greece. *Front Earth Sci.* 9:667160. doi: 10.3389/feart.2021.667160

744 Carranza M, Buforn E, and Zollo A. (2017). Performance of a Network-Based Earthquake  
745 Early Warning system in the Ibero-Maghrebian Region. *Seismol Res Lett*  
746 88(6):1499-1507. doi: 10.1785/0220170081.

747 Caruso A, S. Colombelli, L Elia, M Picozzi, and A Zollo (2017). An on-site alert level  
748 early warning system for Italy. *J Geophys Res* 122, doi:10.1002/2016JB013403.

749 Chung A I, Henson I, and Allen R M (2019). Optimizing Earthquake Early Warning  
750 performance: ElarmS-3. *Seismol Res Lett* 90 (2), doi: 10.1785/0220180192.

751 Chung A I, Meier M A, Andrew J (2020). ShakeAlert Earthquake Early Warning system  
752 performance during the 2019 Ridgecrest earthquake sequence. *Bull seism Soc Am* 110(4),  
753 doi: 10.1785/0120200032.

754 Clinton J, Zollo A, Marmureanu A, Zulfikar C, and Parolai S. (2016). State-of-the art and  
755 future of Earthquake Early Warning in the European region. *Bull Earthquake Eng* 14,  
756 2441-2458. doi: 10.1007/s10518-016-9922-7.

757 Cochran E S, J F Lawrence, C Christensen, and R S Jakka (2009). The QuakCatcher  
758 Network: Citizen science expanding seismic horizons. *Seismol Res Lett* 80, 26-30.

759 Cochran E S, Aagaard B T, Allen R M, Andrews J, Baltay A S, Barbour A J, Bodin P,  
760 Brooks B A, Chung A, Crowell B W, Given D D, Hnaks T C, Hartog J R, Hauksson E,  
761 Heaton T H, MacBride S, Meier M -A, Melgar D, Minson S E, Murray J R, Strauss J A,  
762 and Toomey D, 2018. Research to improve ShakeAlert earthquake early warning products  
763 and their utility: U. S. Geological Survey Open-File Report 2018-1131, 17p.,  
764 <http://doi.org/10.3133/ofr20181131>.

765 Cochran E S, Bunn J, Minson S E, Baltay A S, Kilb D L, Kodera Y, and Hoshiba M (2018).  
766 Event detection and performance of the PLUM Earthquake Early Warning algorithm in  
767 Southern California. *Bull Seismol Soc Am* 109(4), doi: 10.1785/0120180326.

768 Convertito V, M Caccavale, R De Matteis, A Emolo, D J Wald, and A Zollo (2012). Fault  
769 extent estimation for near-real time ground-shaking map computation purposes, *Bull*  
770 *Seismol Soc Am* 102, 578-586, doi:10.1785/0120100306.

771 Cochran E S, and Husker A L (2019). How low should we go when warning for  
772 earthquakes? *Science*, v. 366, p. 957-958, <http://doi.org/10.1126/science.aaz6601>.

773 Colombelli, S., O. Amoroso, A. Zollo, and H. Kanamori (2012). Test of a threshold-based  
774 earthquake early warning using Japanese data, *Bull Seismol Soc Am* 102,1266-1275, doi:  
775 10.1785/0120110149.

776 Cremen G, Zuccolo E, Galasson C (2021). Accuracy and uncertainty analysis of selected  
777 methodological approaches to earthquake early warning in Europe. *Seismol Res Lett*  
778 doi:10.1785/0220200414.

779 Cua G, Heaton T (2007). The Virtual Seismologist (VS) method: a Bayesian approach to  
780 earthquake early warning. In: Gasparini, P. Manfredi, G., Zschau, J (eds) *Earthquake*  
781 *Early Warning systems*. Springer Berlin, pp 85-132.

782 Cua, G, Fischer M, Heaton T, Wiemer S (2009a). Real-time performance of the virtual  
783 seismologist earthquake early warning algorithm in Southern California. *Seismol. Res.*  
784 *Lett.* 80:740-747. doi: 10.1785/gssrl.80.5.740

785 Cua G B. & Heaton T H (2009b). Characterizing average properties of southern California  
786 ground motion amplitudes and envelopes, *Earthquake Engineering Research Laboratory*,  
787 Pasadena, CA. Available at: <http://resolver.caltech.edu/CaltechEERL:EERL-2009-05>,  
788 last accessed June 2017.

789 Doi K. (2011). The operation and performance of earthquake early warnings by the Japan  
790 Meteorological Agency. *Soil Dynamics and Earthquake Engineering*, 31 (2), 119-126.

791 Dokka R K, and C J Travis (1990). Role of the eastern California shear zone in  
792 accommodating Pacific-North American plate motion, *Geophys Res Lett* 17, 1323-1327,  
793 1990.

794 Fleming K, M Picozzi, C Mikereit, F Kuehnlentz, B Liuchtblau, J Fischer, C Zulfikar, O  
795 Oezel, J Zschau, I Zschau, I Veit, K H Jaeckel, M Hoenig, J Nachtigall, H Woith, J P  
796 Redlich, K Ahrens, I Eveslage, S Heglmeier, M Edrik and N Kafadar (2009). Seismic  
797 Early Warning for Europe (SAFER) Working Group (2009) Earthquake Data Information  
798 system for the Marmara Sea (EDIM) Working Group International, The Self-Organizing  
799 Seismic Early Warning Information Network (SOSEWIN). *Seismol Res Lett* 80(5),  
800 755-771.

801 Feng W, Samsonov S, Qiu Q, Wang Y, Zhang P, Li T, & Zheng W. (2020). Orthogonal  
802 fault rupture and rapid postseismic deformation following 2019 Ridgecrest, California,

803 earthquake sequence revealed from geodetic observations. *Geophys Res Lett* 47,  
804 e2019GL086888. <http://doi.org/10.1029/2019GL086888>

805 Gallovê F, Valentova' L', Ampuero J -P, & Gabriel A -A (2019). Bayesian dynamic  
806 finite-fault inversion: 2. Application to the 2016  $M_w$ 6.2 Amatrice, Italy, earthquake.  
807 *Journal of Geophysical Research: Solid Earth*, 124. <http://doi.org/10.1029/2019JB017512>

808 Given D D, Cochran E S, Heaton T, Hauksson E, Allen R, Hellweg P, Vidale J, and Bodin  
809 P, 2014, Technical implement plan for the ShakeAlert production system-An Earthquake  
810 Early Warning system for the West Coast of the United States: U. S. Geological Survey  
811 Open-File Report 2014-1097, 25p., <http://doi.org/10.3133/ofr20141097>.

812 Given D D, Allen R, Baltay A S, Bodin P, Cochran E S, Creager K, Creager K, de Groot R,  
813 Gee L S, Hauksson E, Heaton T H, Hellweg M, Murray J, Thomas V I, Toomey D, and  
814 Yelin T S (2018). Revised technical implementation plan for the ShakeAlert production  
815 system—An earthquake early warning system for the West Coast of the United States, U.  
816 S. Geological Survey Open-File Report 2018-1155, 42p.,  
817 <http://dx.doi.org/10.3133/ofr20181155>. [Supersedes USGS Open-File Report2014-1097.]

818 Grapenthin, R., Johanson, I. A., Allen, R. M. (2014). Operational real-time GPS-enhanced  
819 earthquake early warning. *J. Geophys Res Solid Earth* 119 (10) : 7944-7965.

820 Horiuchi S, Y Horiuchi, S Yamamoto, H Nakamura, C Wu, P Rydelek and M Kachi  
821 (2019). Home seismometer for earthquake early warning, *Geophys Res Lett* 36, L00B04;  
822 doi: 10.1029/2008GL036572.

823 Hsu T -Y, H -H Wang, P -Y Lin, C C -M Lin, C -H Kuo, and K -L Wen (2016).  
824 Performance of the NCREE's on-site warning system during the 5 February 2016  $M_w$   
825 6.53 Meinong earthquake. *Geophys Res Lett* 43, 8954-8959, doi:10.1002/2016GL069372

826 Hudnut K W, B A Brooks, K Scharer, J L Hernandez, T E Dawson, M E Oskin, J Ramon  
827 Arrowsmith, C A Goulet, K Blake, M L Boggs, et al (2020). Airborne Lidar and  
828 Electro-Optical Imagery along surface ruptures of the 2019 Ridgecrest earthquake  
829 sequence, Southern California, *Seismol Res Lett*. XX, 1-12, DOI: 10.1785/0220190338.

830 Iervolino I, Giorgio M, Galasso C, et al (2009). Uncertainty in early warning predictions of  
831 engineering ground motion parameters: What really matters. *Geophys Res Lett* 36 (5):  
832 L00B06, doi: 10.3969/j. issn. 0253-3782. 2012. 05. 002.

833 Juhel K, Ampuero J -P, Barsuglia M, Bernard P, Chassande-Mottin E, Fiorucci D et al  
834 (2018). Earthquake early warning using future generation gravity strainmeters. *Journal of*  
835 *Geophysical Research: Solid Earth*, 123, 10889-10902.  
836 <http://doi.org/10.1029/2018JB016698>.

837 Iervolino I (2011). Performance-based earthquake early warning. *Soil Dyn Earthq Eng.*  
838 31(2), 209-222.

839 Kanamori H, Maechling P, and Hauksson E (1999). Continuous monitoring of  
840 ground-motion parameters, *Bull. Seism. Soc. Am.* 89,311-316.

841 Kawamoto S, Ohta Y, Hiyama Y, Todoriki M, Nishimura T et al (2017). REGARD: a new  
842 GNSS-based real-time finite fault modeling system for GEONET. *J. Geophys. Res. Solid*  
843 *Earth* 122 (2): 1324-1349.

844 Li J, Böse M, Feng Y and Yang C. (2021) Real-Time characterization of finite rupture and  
845 its implication for Earthquake Early Warning: application of FinDer to existing and  
846 planned stations in Southwest China. *Front Earth Sci.* 9:699560. doi:  
847 10.3389/feart.2021.699560

848 Liu A, Yamada M. 2014. Bayesian approach for identification of multiple events in an  
849 early warning system. *Bull Seismol Soc Am* 104(3): 1111-21.

850 Liu-Zeng J, T Heaton, and C DiCaprio (2005). The effect of slip variability on earthquake  
851 slip-length scaling. *Geophys J Int* 162(3), 841-840.

852 Manighetti I, Campillo M, Sammis C, Mai P, and King G (2005). Evidence for self-similar,  
853 Triangular slip distributions on Earthquakes: implications for earthquake and fault  
854 mechanics. *J. Geophys. Res. Solid Earth* 110. doi:10.1029/2004jb003174.

855 Manighetti I, Campillo M, Bouley S, and Cotton F. (2007). Earthquake scaling, fault  
856 segmentation, and structural maturity. *Earth Planet Sci Lett* 253, 429-438.  
857 doi:10.1016/j.epsl.2006.11.004.

858 Massin F, Clinton J, and Böse M (2021). Status of Earthquake Early Warning in  
859 Switzerland. *Front. Earth. Sci.* 9.707654. doi: 10.3389/feart.2021.707654

860 McGuire J J, Smith D E, Frankel A D, Wirth E A, McBride S K, and de Groot R M (2021a).  
861 Expected warning times from the ShakeAlert earthquake early warning system for  
862 earthquakes in the Pacific Northwest (ver. 1.1, March 24 2021): U. S. Geological Survey  
863 Open-File Report 2021-1026, 37p., <http://doi.org.10.3133/ofr20211026>

864 McGuire J J, Minson S E, Murray J R, & Brooks B A. (2021b). Commentary: The role of  
865 geodetic algorithms for earthquake early warning in Cascadia. *Geophys Res Lett* 48,  
866 e2020GL092324. <http://doi.org/10.1029/2020GL092324>.

867 Meier M -A, Heaton T, Clinton J. (2015). The Gutenberg algorithm: evolutionary  
868 Bayesian magnitude estimates for earthquake early warning with a filter bank. *Bull*  
869 *Seismol Soc Am.* 105(5): 27774-86.

870 Meier M -A, Ross Z E, Ramachandran A, Balakrishna A, Nair S, Kundzicz P, et al  
871 (2019). Reliable real-time seismic signal/noise discrimination with machine learning.  
872 Journal of Geophysical Research: Solid Earth 124, 788-800.  
873 <http://doi.org/10.1029/2018JB016661>.

874 Meier M A, J P Ampuero and T H Heaton (2017a). The hidden simplicity of subduction  
875 megathrust earthquakes. Science 357, no. 6357, 1277-1281, doi:  
876 10.1126/science.aan5643.

877 Meier M A (2017b). How “good” are real-time ground motion predictions from  
878 earthquake early warning systems? J Geophys Res : Solid Earth 122, no. 7, 5561-5577.

879 Meier M A, Y Kodera, M Böse, A Chung, M Hoshihara, E Cochran, S Minson, E Hauksson  
880 and T Heaton (2020a). How often can Earthquake Early Warning systems alert sites with  
881 high intensity ground motion? J. Geophys. Res. : Solid Earth, 125, doi:  
882 10.1029/2019JB017718.

883 Meier M -A, Ampuero J -P, Cochran E, and Page M. (2020). Apparent Earthquake  
884 Rupture Predictability. Geophys. J. Int. Ggaa610. 225,657-663.doi:10.1093/gji/ggaa610

885 Melgar D, Hayes GP. (2017). Systematic observations of the slip pulse properties of large  
886 earthquake ruptures. Geophys Res Lett 44 (19) : 9691-9698.

887 Minson S E, Murray J R, Langbein J O, Gomberg J S (2014). Real-time inversions for  
888 finite fault slip models and rupture geometry based on high-rate GPS data. J Geophys Res  
889 Solid Earth 119 (4) : 3201-3231.

890 Minson S E, Meier M A, Baltay A S, Hanks T C, & Cochran E S. (2018). The limits of  
891 earthquake early warning: Timeliness of ground motion estimates,. Sci. Adv. 4 (3),  
892 eaaq0504, <https://doi.org/10.1126/sciadv.aaq0504>.

893 Minson S E, A S Baltay, E S Cochran, T C Hans, M T Page, S K McBride, K R Milner,  
894 and M A Meier (2019). The limits of Earthquake Early Warning accuracy and best alerting  
895 strategy. Sci. Rep., 9, doi.org/10.1038/s41598-019-39384-y.

896 Nof R N, and R M Allen (2016). Implementing the ElarmS Earthquake Early Warning  
897 algorithm on the Israeli seismic network. Bull Seismol Soc Am 106(5), 1-13 doi:  
898 10.1785/0120160010.

899 Olson E, and R M Allen (2005). The deterministic nature of earthquake rupture. Nature  
900 438, 212-215.

901 Parolai S, Bindi D, Boxberger T, Milkereit C, Fleming K, Pittore M (2015a). On-site early  
902 warning and rapid damage forecasting using single stations : outcomes from the REAKT  
903 project. Seismol Res Lett 86(5): 1393-1404, doi:10.1785/0220140205

904 Picozzi M, C Milkereit, S Parolai, K -H Jaeckel, I Veit, J Fischer, and J Zschau (2010).  
905 GFZ Wireless Seismic Array (GFZ-WISE), a Wireless Mesh Network of Seismic Sensors:  
906 New Perspectives for Seismic Noise Array Investigations and Site Monitoring, *Sensors*,  
907 10, 3280-3304; doi: 10.3390/s100403280.

908 Picozzi M, A Zollo, P Brondi, S Colombelli, L Elia, and C Martino (2015). Exploring the  
909 feasibility of a nationwide earthquake early warning system in Italy. *J Geophys Res Solid*  
910 *Earth* 120, doi: 10.1002/2014JB011669

911 Picozzi M, D Bindi, P Brondi, D Di Giacomo, S Parolai, and A Zollo (2017).  
912 determination of P wave-based energy magnitude: Insights on source parameter scaling of  
913 the 2016 Central Italy earthquake sequence, *Geophys Res Lett* 44, 4036-4045, doi:  
914 10.1002/2017GL073228.

915 Kamigaichi O, M Saito, K Doi, T Matsumori, S Tsukada, K Takeda, T Shimoyama, K  
916 Nakamura, M Kiyomoto, and Y Watanabe (2009). Earthquake early warning in Japan :  
917 Warning the general public and future prospects, *Seismol Res Lett* 80, no. 5, 717-726,  
918 doi:10.1785/gssrl.80.5.717.

919 Kanamori H (2005). Real-time seismology and earthquake damage mitigation, *Annu. Rev.*  
920 *Earth Planet. Sci.* 33, no. 1, 195-214, doi:10.1146/annurev.earth.33.092203.122626.

921 Kodera Y, Saitou J, Hayashimoto N, Adachi S, Morimoto M, Nishimae Y, and Hoshiba M  
922 (2016). Earthquake early warning for the 2016 Kumamoto earthquake-Performance  
923 evaluation of the current system and the next-generation methods of the Japan  
924 Meteorological Agency: *Earth Planets and Space* v.6, no. 202,  
925 <https://doi.org/10.1186/s40623-016-0567-1>.

926 Kohler M D, Cochran E S, Given D, Guiwits S, Neuhauser D, Henson I, Hartog R, Bodin  
927 P, Kress V, Thompso S, Felizardo C, Brody J, Bhadha R, and Schwarzand S (2018).  
928 Earthquake Early Warning ShakeAlert System—West Coast Wide Production Prototype:  
929 *Seismol Res Lett* v. 89, no. 1. p. 99-107.

930 Kong Q, R M Allen, L Schreier, and Y -W Kwon (2016). MyShake: A smartphone seismic  
931 network for earthquake early warning and beyond, *Sci Adv* 2, e1501055.

932 Kuyuk H S, and R M Allen (2013). Optimal seismic network density for earthquake early  
933 warning : A case study from California, *Seismol Res Lett* 84, no. 6, 946-954, doi:  
934 10.1785/0220130043

935 Liu A & Yamada M (2014). Bayesian approach for identification of multiple events in an  
936 early warning system. *Bull Seism Soc Am* 104(3). doi:10.1785/0120130208.

937 McGuire J J, Smith D E, Frankel A D, Wirth E A, McBride S K, and de Groot R M (2021).  
938 Expected warning times from the ShakeAlert earthquake warning system for earthquakes

939 in the Pacific Northwest (ver. 1.1, March 24, 2021): U.S. Geological Survey Open-File  
940 Report 2021-1026, 37p., <http://doi.org/10.3133/ofr20211026>.

941 McGuire J J, Minson S E, Murray J R, & Brooks B A (2021b). Commentary: The role of  
942 geodetic algorithms for early warning in Cascadia. *Geophys Res Lett*, 48,  
943 e2020GL092324. <http://doi.org/10.1029/2020GL092324>.

944 Minson S E, S Wu, J L Beck, and T H Heaton (2017). Combining multiple earthquake  
945 models in real time for earthquake early warning. *Bull Seismol Soc Am* Doi:  
946 10.1785/0120160331.

947 Minson S E, Meier M A, Baltay A S, Hanks T C, & Cochran E S (2018). The limits of  
948 earthquake early warning: Timeliness of ground motion estimates,. *Sci Adv* 4 (3),  
949 eaaq0504, <https://doi.org/10.1126/sciadv.aaq0504>.

950 Miller M M, Johnson D J, Dixon T H & Dokka R K (2001). Refined kinematics of the  
951 eastern California shear zone from GPS observations, 1993-1998, *J geophys Res*  
952 106(B2), 2245-2263.

953 Milliner C, and A Donnellan (2020). Using daily observations from planet labs satellite  
954 imagery to separate the surface deformation between the 4 July Mw 6.4 Foreshock and 5  
955 July Mw 7.1 Mainshock during the 2019 Ridgecrest earthquake sequence. *Seismol Res*  
956 *Lett* doi: 10.1785/0220190271.

957 Minson S E, A S Baltay, E S Cochran, T C Hans, M T Page, S K McBride, K R Milner,  
958 and M A Meier (2019). The limits of Earthquake Early Warning accuracy and best alerting  
959 strategy. *Sci Rep* 9, doi.org/10.1038/s41598-019-39384-y.

960 Mori J, & Helmberger D (1996). Large-amplitude moho reflections (SmS) from Landers  
961 aftershocks, Southern California. *Bull Seismol Soc Am* 86, 1845-1852 (1996).

962 Olivieri M, Allen R M, and Wurman G (2008). The potential for Earthquake Early  
963 Warning in Italy using ElarmS. *Bull Seismol Soc Am* 98(1), 495-503 (2008).  
964 doi:10.1785/0120070054

965 Ross Z E, B Idini, Z Jia, O L Stephenson, M Zhong, X Wang, Z Zhan, M Simons, E J  
966 Fielding, S -H Yun, et al (2019). Hierarchical interlocked orthogonal faulting in the 2019  
967 Ridgecrest earthquake sequence, *Science* 366, no. 6463, 346-351, doi:  
968 10.1126/science.aaz0109.

969 Ruhl C J, Melgar D, Grapenthin R, & Allen R M (2017). The value of real-time GNSS to  
970 earthquake early warning. *Geophys Res Lett*, 44, 8311-8319.  
971 <http://doi.org/10.1002/2017GL074502>.

972 Ruhl C J, Melgar D, Chung A I, Grapenthin R, & Allen R M (2019). Quantifying the value  
973 of real-time geodetic constraints for Earthquake Early Warning using a glabal seismic and

974 geodetic data set. *Journal of Geophys Research: Solid Earth* 124(4), 3819-3837.  
975 <http://doi.org/10.1002/2017GL074502>

976 Sauber J, W Thatcher, S C Solomon and M Lisowski. Geodetic slip rate for the Eastern  
977 California Shear Zone and the recurrence time of Mojave desert earthquakes. *Nature* 367,  
978 264-266, 1994.

979 Sadeh M. Ziv A, and Wust-Bloch H (2014). Real-time magnitude proxies for earthquake  
980 early warning in Israel. *Geophys J Int.* 196, 939-950. doi: 10.1093/gji/ggt407.

981 Shelly D R (2020). A high-resolution seismic catalog for the initial 2019 Ridgecrest  
982 earthquake sequence: Foreshocks, aftershocks and faulting complexity. *Seismol Res Lett*,  
983 1-8. <http://doi.org/10.1785/0220190309>

984 Sokos E, Tselentis G -A, Paraskevopoulos P, Serpersidaki A, Stathopoulos-Valamis A,  
985 and Pannagis A (2016). Towards Earthquake Early Warning for the Rion-Antiron Bridge,  
986 Greece. *Bull Earthquake Eng* 14, 2531-2542. doi:10.1007/s10518-016-9893-8

987 Stewart J P et al (2019). Preliminary report on engineering and geological effects of July  
988 2019 Ridgecrest Earthquake sequence: Geotechnical Extreme Events Reconnaissance  
989 Association Report GEER-064,<http://doi.org/10.18118/G6H66K>

990 Stubailo I, Alvarez M, Biasi G, Bhadha R, and Hauksson E (2020). Latency of waveform  
991 data delivery from the Southern California seismic network during the 2019 Ridgecrest  
992 earthquake sequence and its effect on ShakeAlert: *Seismol Res Lett* v. 92, p. 170-186,  
993 <http://doi.org/10.1785/0220200211>.

994 Trugman D T, Page M T, Minson S E, & Cochran E S (2019). Peak ground displacement  
995 saturates exactly when expected: Implications for earthquake early warning. *Journal of*  
996 *Geophysical Research: Solid Earth*, 124, 4642-4653.  
997 <http://doi.org/10.1029/2018JB017093>

998 S.Geological Survey (USGS), 2019. Available at:  
999 <http://earthquake.usgs.gov/earthquakes/eventpage/ci38443183/executive>.

1000 Wald D J, V Quitoriano, T H Heaton, and H Kanamori (1999). Relationships between  
1001 peak ground acceleration, peak ground velocity, and modified Mercalli intensity in  
1002 California, *Earthquake spectra* 15, no. 3, 557-564.

1003 Wald D J (2020). Practical Limitations of earthquake early warning: *Earthquake Spectra* v.  
1004 36, p. 1412-1447, <http://doi.org/10.1177/8755293020911388>.

1005 Wang K, and Bürgmann R, (2020a). Co- and Early Postseismic Deformation Due to the  
1006 2019 Ridgecrest Earthquake Sequence Constrained by Sentinel-1 and COSMO-SkyMed  
1007 SAR Data. *Seismol Res Lett* 91,1998-2009,doi:10.1785/0220190299

1008 Wang K, D S Dreger, E Tinti, R Bürgmann, and T Taira (2020b). Rupture process of the  
1009 2019 Ridgecrest, California  $M_w$ 6.4 Foreshock and  $M_w$ 7.1 earthquake constrained by  
1010 seismic and geodetic data. *Bull Seismol Soc Am* XX, 1-24, doi: 10.1785/0120200108

1011 Wells D L, and K J Coppersmith (1994). New empirical relationships among magnitude,  
1012 rupture length, rupture width, rupture area, and surface displacement. *Bull Seismol Soc*  
1013 *Am* 84, no. 4, 974-1002.

1014 Wu Y M, Kanamori H (2005). Experiment on an onsite early warning method for the  
1015 Taiwan early warning system. *Bull Seismol Soc Am* 95(1), 347-353.

1016 Wu Y -M, H Kanamori, R M Allen, and E Hauksson (2007). Determination of earthquake  
1017 early warning parameters,  $\tau_c$  and  $P_d$ , for southern California, *Geophys J Int* 170,  
1018 711-717, doi: 10.1111/j.1365-246X. 3732007. 03430.x

1019 Wu Y -M, D -Y Chen, T -L Lin, C -Y Hsieh, T -L Chin, W -Y Chang, W -S Li, and S -H  
1020 Ker (2013). A high-density seismic network for earthquake early warning in Taiwan based  
1021 on low cost sensors, *Seismol Res Lett*, 84(6), 1048-1054.

1022 Wurman G, R M Allen, and P Lombard (2007). Toward earthquake early warning in  
1023 northern California. *J Geophys Res* 112, no. B08311, doi: 10.1029/2006JB004830

1024 Zollo A, Amoroso O, Lancieri M, Wu Y M, Kanamori H (2010). A threshold-based  
1025 earthquake early warning using dense accelerometer networks. *Geophys J Int* 183:  
1026 963-974

1027 Zollo A, S Colombelli, L Elia, A Emolo, G Festa, G Iannaccone, C Martino, and P  
1028 Gasparini (2014). An integrated regional and on-site Earthquake Early Warning System  
1029 for Southern Italy: Concepts, methodologies and performances, in *Early Warning for*  
1030 *Geological Disasters—Scientific Methods and Current Practices*, edited by F Wenzel, and  
1031 J Zschau, pp. 117-137, Springer, Berlin.

1032

1033 **TABLE CAPTIONS**

1034 **Table 1** Basic source information and finite-source results during the 2019, Ridgecrest  
1035 earthquake sequence

1036 **TABLES**

**Table 1****Basic source information and final finite-source results for the 2019 Ridgecrest earthquake sequence ( $M \geq 5.0$ )**

Even. ID <sup>†</sup>	Origin Time(UTC) (yyyy/mm/dd hh:mm:ss)	Epicenter <sup>†</sup>			$M_w^*/M_L^†$	Strike/Dip/Rake* (°)	$D_i / \Gamma$ (km/°)	FinDer		
		Latitude (°)	Longitude (°)	Focal Depth (km)				L (km)	$\Theta$ (°)	M
ci38457511	2019/07/06 03:19:53	35.7695	-117.5993	8.0	7.1	322/81/-173	12.3/30	54/50 <sup>‡</sup>	136 <sup>§</sup>	6.9
ci38443183	2019/07/04 17:33:49	35.7052	-117.5060	10.7	6.4	137/86/156	20.2/30	29/20 <sup>‡</sup>	120	6.5
ci38450263	2019/07/05 11:07:53	35.7603	-117.5750	7.0	5.4	313/75/-159	12.8/30	6	117 <sup>§</sup>	5.5
ci38457487	2019/07/06 03:16:32	35.7253	-117.5535	0.9	5.0	226/74/-8	14.0/60	2	179	4.8

ci37219164	2019/07/06 03:23:50	35.8002	-117.6052	12.4	4.8/5.4	-	25.8/75	0.44	150	3.8
ci38457687	2019/07/06 03:47:53	35.9030	-117.7458	3.4	5.5/5.0	336/84/-160	28.3/60	1.3	113 <sup>§</sup>	4.5
ci38457775	2019/07/06 04:07:04	35.5553	-117.5237	5.6	4.7/5.0	270/71/-64	15.9/45	1.3	125 <sup>§</sup>	4.5
ci38457847	2019/07/06 04:18:55	35.910	117.685	7.4	5.4	339/76/-155	30.1/45	1.3	145 <sup>§</sup>	4.5

---

1038 † Obtained from CESMD (Center for Engineering Strong Motion Data). (see Data and Resources)

1039 \* Obtained from USGS (United States Geological Survey). (see Data and Resources)

1040 ‡ Wang et al. (2020b)

1041 § the azimuth of rupture is equivalent to  $\Theta + 180^\circ$  due to symmetry

1042  $D_i$ , interstation distance (Li et al., 2021);  $\Gamma$ , degree of sparseness (Convertito et al., 2012)

1043  $L$ , rupture length;  $\Theta$ , rupture azimuth;  $M$ , magnitude determined by L-M scaling relationship (Wells & Coppersmith, 1994)

1044

1045

1046

1047

1048

1049

1050

1051

1052

1053

1054

1055

1056

1057

1058

1059

1060

1061

1062

1063

1064

1065

1066

1067 **FIGURE CAPTIONS**

1068 **Fig. 1** The red lines projected on the focal spheres illustrate the FinDer results of rupture  
1069 strike for seven earthquakes. The gray squares mark the seismic stations deployed within  
1070 the research region. Blue stars mark the epicenter, the reference focal mechanisms are  
1071 derived from USGS (see data and resource). The black lines mark the quaternary faults  
1072 derived from USGS Quaternary Fault & Fold Database (see data and resource). (b), The  
1073 temporal evolution of rupture length and magnitude through time as determined by FinDer  
1074 for three respective events. (c), Colored circles show the time from earthquake origin to  
1075 the time of the MMI 3.5 alert contour determined by FinDer for three respective events.  
1076 Red and yellow triangles denote the time a particular site exceeds MMI 3.5 and 4.5,  
1077 respectively. Black lines show the move out speed of 2, 3, 4, 8 and 10 kilometers per  
1078 second (*km/s*).

1079 **Fig. 2** Temporal alert performance for  $M_w$ 7.1 Ridgecrest, California earthquake assuming  
1080 zero data processing and alert transmission latency. (a)-(f) FinDer detects the event 3.5 s  
1081 after origin time and updates source parameters estimates in 0.5 s interval for about 23.5 s;  
1082 The black lines show the optimum line-source model determined by FinDer at certain  
1083 point of time. The yellow star marks the epicenter. We use squares to denote sites that  
1084 would have been alerted since the maximum predicted ground motion intensities has  
1085 overcome the alert threshold of  $MMI_{alert} = 3.5$  using the GMPEs of BA08 (Boore et al.,  
1086 2008; Atkinson and Boore, 2011) and the GMICE of Wald et al. (1999) assuming rock  
1087 condition. Whereas, the triangles are sites that have not yet received alert.

1088 **Fig. 3** Examples of the MMI threshold alert performance as a function of warning time for  
1089 each individual site. We illustrate two or four example sites for three respective events.  
1090 Gray shaded region enclosed by the black and red curves shows the warning time based on  
1091 the alert criterion of  $MMI_{alert}$  3.5. Warning time is regard as the time difference between  
1092 the time the predicted ground motion intensity for the first time overcomes the alert  
1093 threshold and the time the observed ground motion intensity reaches the damage threshold  
1094  $MMI_{tw}$  3.5. The station code, hypocentral distance and warning time (*wt*) are shown in top  
1095 right corner of each figure.

1096 **Fig. 4** Warning time map for three respective events, the colored lines illustrate the  
1097 simplified contours of peak observed MMI intensity applying the alert criterion of  
1098  $MMI_{alert}$  3.5. Warning time is regarded as the time difference between the time the  
1099 predicted ground motion intensity for the first time overcomes the alert threshold and the  
1100 time the observed ground motion intensity reaches the damage threshold  $MMI_{tw} = 3.5$ .  
1101 The contour lines are plotted by exploiting Matlab's Natural Neighbor interpolation  
1102 strategy. The yellow star denotes the epicenter, the blue line is the final optimum line  
1103 source determined by FinDer algorithm.

1104 **Fig. 5** (a)-(c), Real-time alert classification results for the total earthquake sequence by  
1105 applying the alert criterion of  $MMI_{\text{alert}} = 2.5, 3.5, \text{ and } 4.5$ , the damage threshold is  
1106 equivalent to the corresponding alert threshold. Each site is colored according to the  
1107 warning time; Quadrants are classified as true positive (TP), true negative (TN), false  
1108 positive (FP), or false negative (FN). The bars at the bottom show the fractions of case for  
1109 true and false alerts; Blue lines give *5th*, *50th*, and *95th* percentiles in bins of observed  
1110 MMI intensity.

1111 **Fig. 6** (a), Real-time alert classification results without TN cases using six choices of alert  
1112 criteria. Percentages of true positive (TP), false positive (FP), and false negative (FN)  
1113 alerts are shown in the quadrants; (b), Normalized Cost Reduction Performance Metrics  
1114 CR as a function of cost ratio  $r$  for FinDer real-time classification results using three  
1115 choices of alert criteria.

1116 **Fig. 7** (a)-(c), Empirical cumulative distribution functions (CDF) as a function of warning  
1117 times for sites that should have been alerted in different ground motion intensity bins  
1118 ( $2.5:1:9.5$ ) for the total earthquake sequence, Number of correctly alerted sites and the  
1119 total sites per intensity bin ( $m/n$ ) illustrated as legends are labeled in the top right corner of  
1120 each figure. The results are shown for three different alert threshold, the damage threshold  
1121 is equivalent to the corresponding alert threshold. (a')-(c'), Warning time as a function of  
1122 hypocentral distance. Each site with above threshold amplitude is colored according the  
1123 observed MMI ground motion intensity, the red dots falling on the abscissa show cases  
1124 which should have been alerted but failed to do, and the red stars denote the median  
1125 warning time for different distance bins with the interval of 20 km.

1126 **Fig. 8** Follow the Fig. 7, but the damage threshold is set to MMI 4.5.

1127 **Fig. 9** (a)-(d), Ground motion prediction errors as a function of warning time for three  
1128 respective events and the total earthquake sequence. Warning time is defined as the time  
1129 relative to when the damage threshold is reached for the first time at each individual sites  
1130 or the theoretical S arrival ( $t_s$ ) for sites with blow-threshold amplitudes. The curves are  
1131 colored according to the observed peak MMI value for each recording site. Black lines  
1132 illustrate the 5th, 50th, and 95th percentiles at each point of warning time for alert criterion  
1133 of  $MMI_{\text{alert}} 3.5$ ; Blue line in figure (d) shows the median warning time for alert criterion of  
1134  $MMI_{\text{alert}} = 2.5, MMI_{\text{tw}} = 4.5$ . (e)-(f), the medians for each point of warning time are shown  
1135 for each intensity bin ( $1.5:1:8.5$ ), the curves are colored according to the corresponding  
1136 intensity bin.

1137

1138

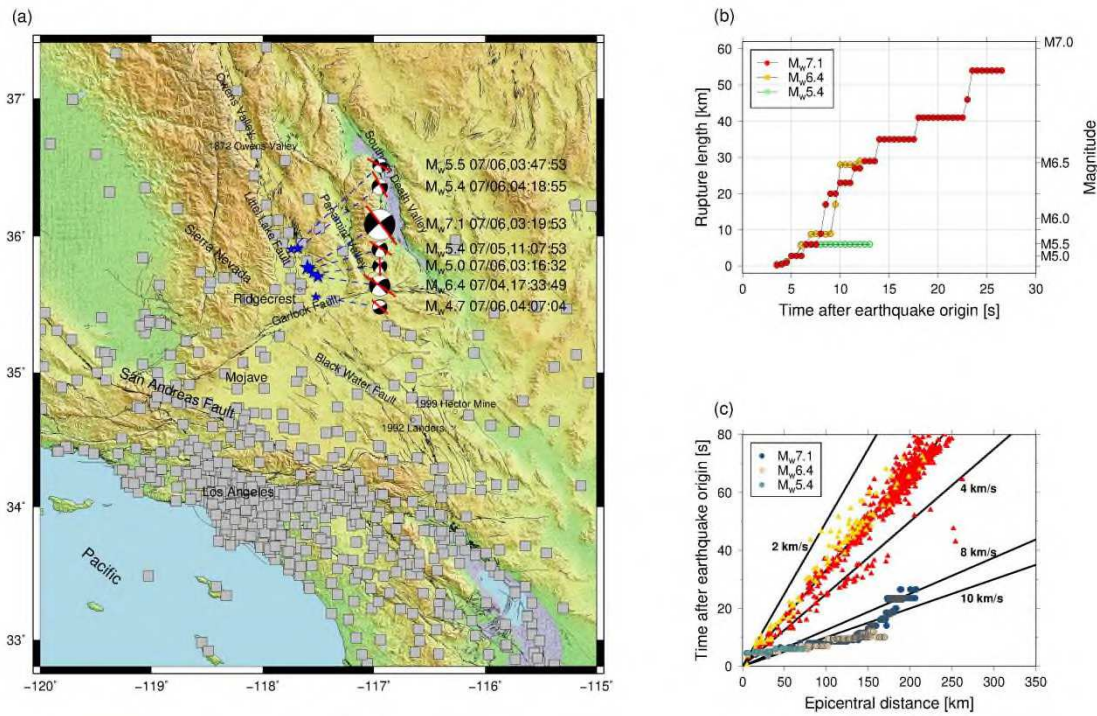
1139

1140

Natural Hazards

1141 FIGURES

1142



1143

1144 **Fig. 1** The red lines projected on the focal spheres illustrate the FinDer results of rupture  
 1145 strike for seven earthquakes. The gray squares mark the seismic stations deployed within  
 1146 the research region. Blue stars mark the epicenter, the reference focal mechanisms are  
 1147 derived from USGS (see data and resource). The black lines mark the quaternary faults  
 1148 derived from USGS Quaternary Fault & Fold Database (see data and resource). (b), The  
 1149 temporal evolution of rupture length and magnitude through time as determined by FinDer  
 1150 for three respective events. (c), Colored circles show the time from earthquake origin to  
 1151 the time of the MMI 3.5 alert contour determined by FinDer for three respective events.  
 1152 Red and yellow triangles denote the time a particular site exceeds MMI 3.5 and 4.5,  
 1153 respectively. Black lines show the move out speed of 2, 3, 4, 8 and 10 kilometers per  
 1154 second (*km/s*).

1155

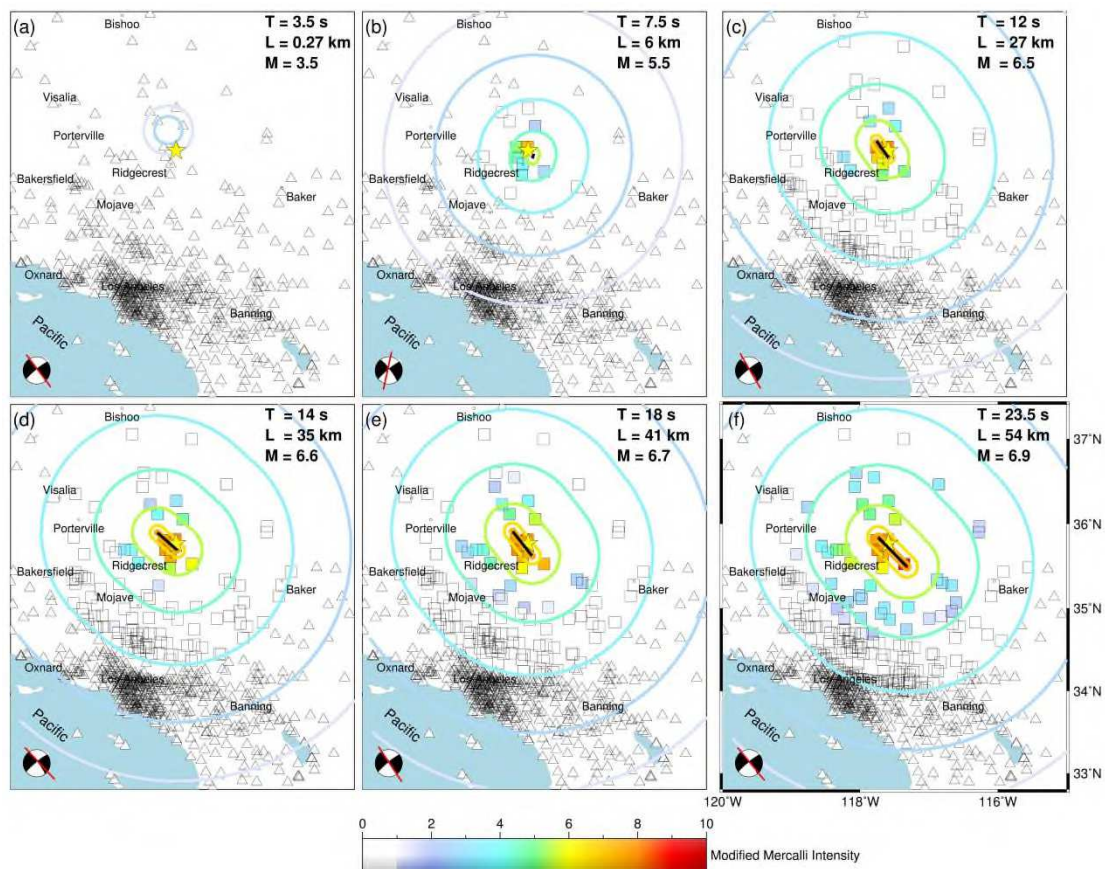
1156

1157

1158

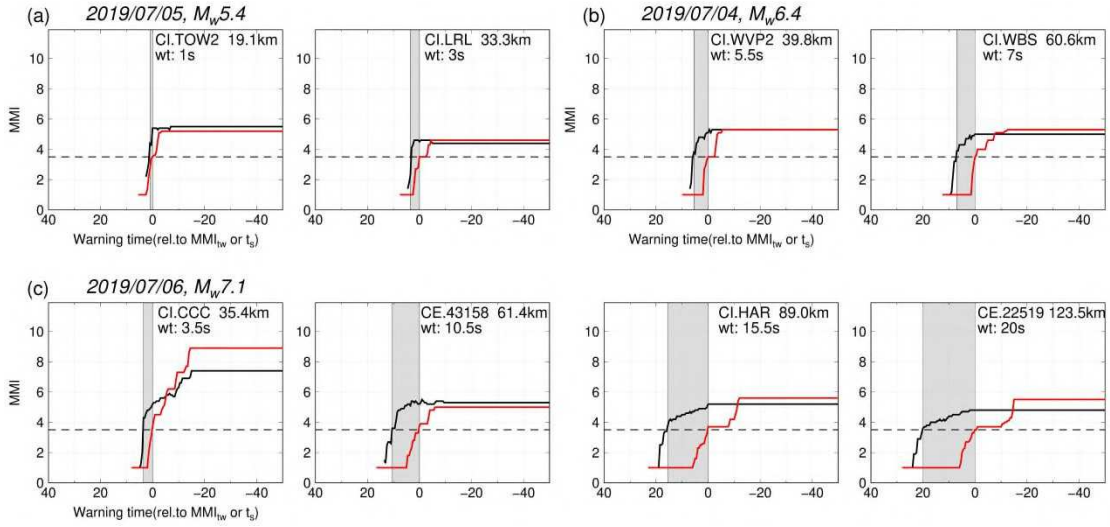
1159

1160



1161

1162 **Fig. 2** Temporal alert performance for  $M_w$  7.1 Ridgecrest, California earthquake assuming  
1163 zero data processing and alert transmission latency. (a)-(f) FinDer detects the event 3.5 s  
1164 after origin time and updates source parameters estimates in 0.5 s interval for about 23.5 s;  
1165 The black lines show the optimum line-source model determined by FinDer at certain  
1166 point of time. The yellow star marks the epicenter. We use squares to denote sites that  
1167 would have been alerted since the maximum predicted ground motion intensities has  
1168 overcome the alert threshold of  $MMI_{\text{alert}} = 3.5$  using the GMPEs of BA08 (Boore et al.,  
1169 2008; Atkinson and Boore, 2011) and the GMICE of Wald et al. (1999) assuming rock  
1170 condition. Whereas, the triangles are sites that have not yet received alert.



1171

1172 **Fig. 3** Examples of the MMI threshold alert performance as a function of warning time for  
 1173 each individual site. We illustrate two or four example sites for three respective events.  
 1174 Gray shaded region enclosed by the black and red curves shows the warning time based on  
 1175 the alert criterion of  $MMI_{alert}$  3.5. Warning time is regard as the time difference between  
 1176 the time the predicted ground motion intensity for the first time overcomes the alert  
 1177 threshold and the time the observed ground motion intensity reaches the damage  
 1178 threshold  $MMI_{tw}$  3.5. The station code, hypocentral distance and warning time ( $wt$ ) are shown in top  
 1179 right corner of each figure.

1180

1181

1182

1183

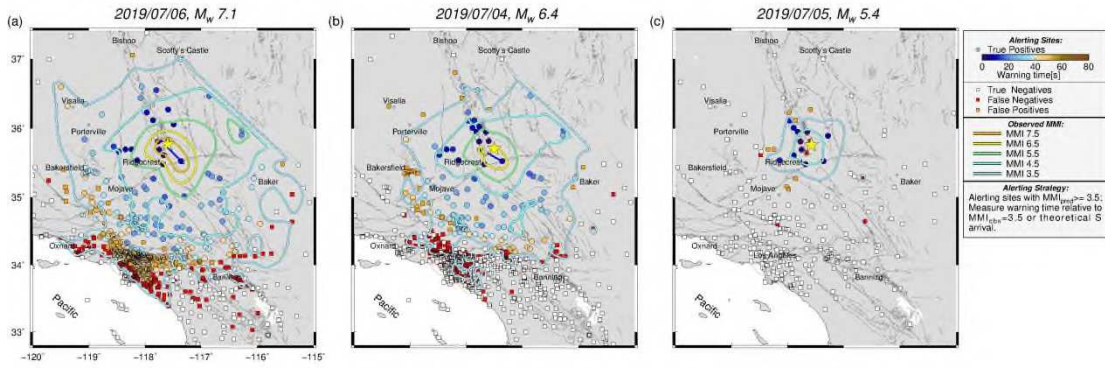
1184

1185

1186

1187

1188



1189

1190 **Fig. 4** Warning time map for three respective events, the colored lines illustrate the  
 1191 simplified contours of peak observed MMI intensity applying the alert criterion of  
 1192  $MMI_{alert} = 3.5$ . Warning time is regarded as the time difference between the time the  
 1193 predicted ground motion intensity for the first time overcomes the alert threshold and the  
 1194 time the observed ground motion intensity reaches the damage threshold  $MMI_{tw} = 3.5$ .  
 1195 The contour lines are plotted by exploiting Matlab's Natural Neighbor interpolation  
 1196 strategy. The yellow star denotes the epicenter, the blue line is the final optimum line  
 1197 source determined by FinDer algorithm.

1198

1199

1200

1201

1202

1203

1204

1205

1206

1207

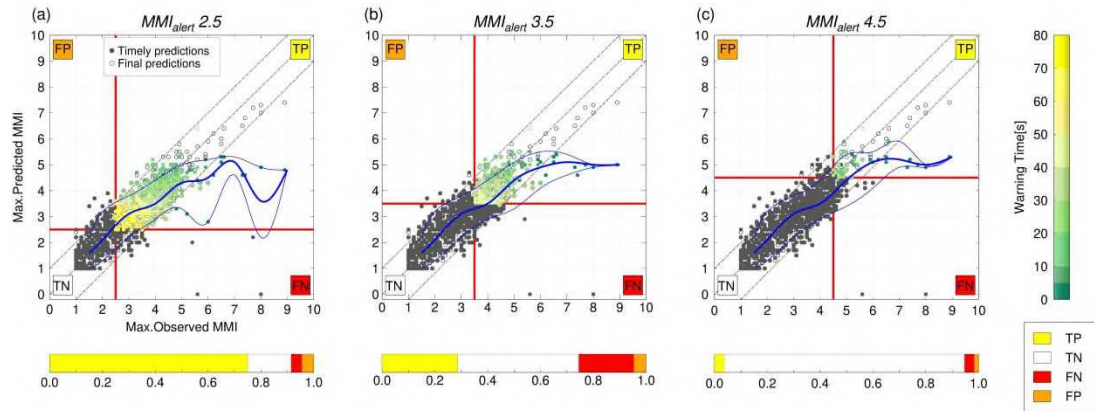
1208

1209

1210

1211

1212



1213

1214 **Fig. 5** (a)-(c), Real-time alert classification results for the total earthquake sequence by  
1215 applying the alert criterion of  $MMI_{alert} = 2.5, 3.5,$  and  $4.5,$  the damage threshold is  
1216 equivalent to the corresponding alert threshold. Each site is colored according to the  
1217 warning time; Quadrants are classified as true positive (TP), true negative (TN), false  
1218 positive (FP), or false negative (FN). The bars at the bottom show the fractions of case for  
1219 true and false alerts; Blue lines give 5th, 50th, and 95th percentiles in bins of observed  
1220 MMI intensity.

1221

1222

1223

1224

1225

1226

1227

1228

1229

1230

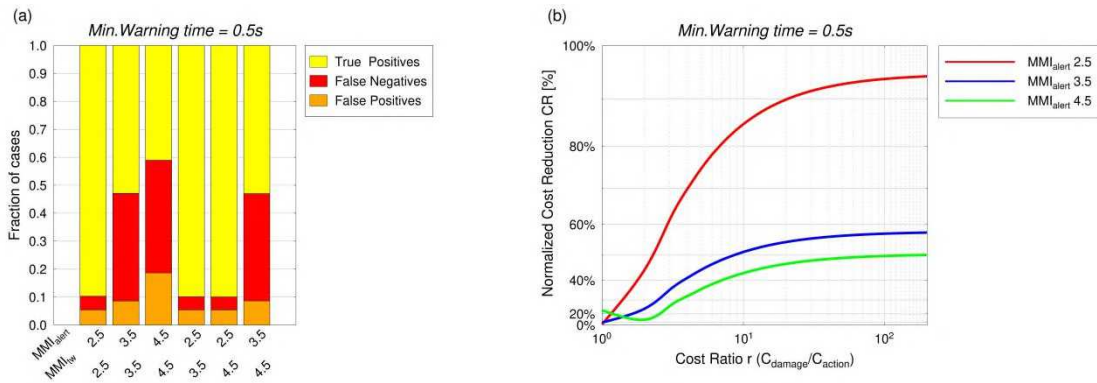
1231

1232

1233

1234

1235



1236

1237 **Fig. 6** (a), Real-time alert classification results without TN cases using six choices of alert  
 1238 criteria. Percentages of true positive (TP), false positive (FP), and false negative (FN)  
 1239 alerts are shown in the quadrants; (b), Normalized Cost Reduction Performance Metrics  
 1240 CR as a function of cost ratio  $r$  for FinDer real-time classification results using three  
 1241 choices of alert criteria.

1242

1243

1244

1245

1246

1247

1248

1249

1250

1251

1252

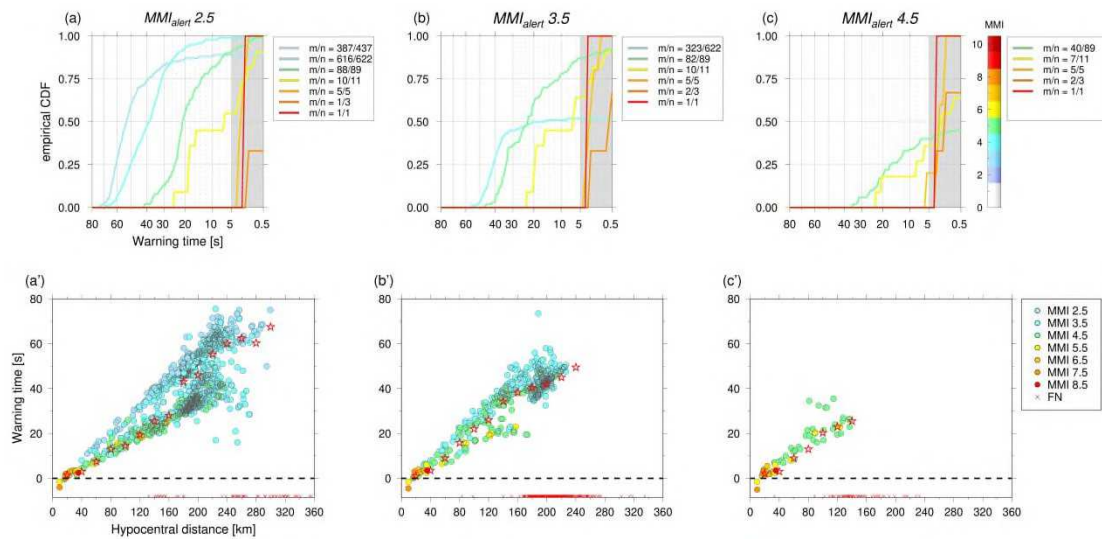
1253

1254

1255

1256

1257



1258

1259 **Fig. 7** (a)-(c), Empirical cumulative distribution functions (CDF) as a function of warning  
 1260 times for sites that should have been alerted in different ground motion intensity bins  
 1261 (2.5:1:9.5) for the total earthquake sequence, Number of correctly alerted sites and the  
 1262 total sites per intensity bin ( $m/n$ ) illustrated as legends are labeled in the top right corner of  
 1263 each figure. The results are shown for three different alert threshold, the damage threshold  
 1264 is equivalent to the corresponding alert threshold. (a')-(c'), Warning time as a function of  
 1265 hypocentral distance. Each site with above threshold amplitude is colored according the  
 1266 observed MMI ground motion intensity, the red dots falling on the abscissa show cases  
 1267 which should have been alerted but failed to do, and the red stars denote the median  
 1268 warning time for different distance bins with the interval of 20 km.

1269

1270

1271

1272

1273

1274

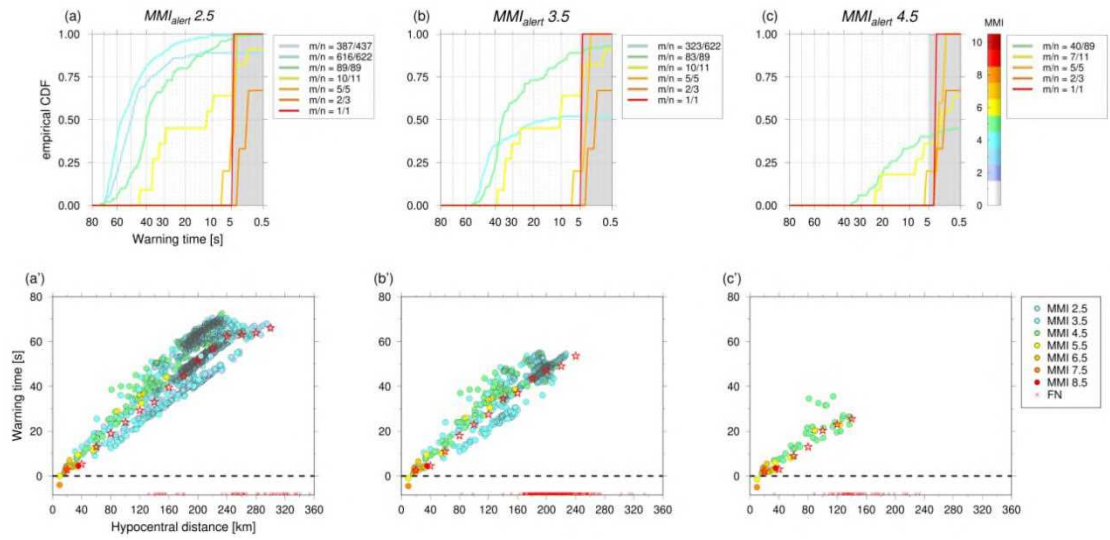
1275

1276

1277

1278

1279



1280

1281 **Fig. 8** Follow the Fig. 7, but the damage threshold is set to MMI 4.5.

1282

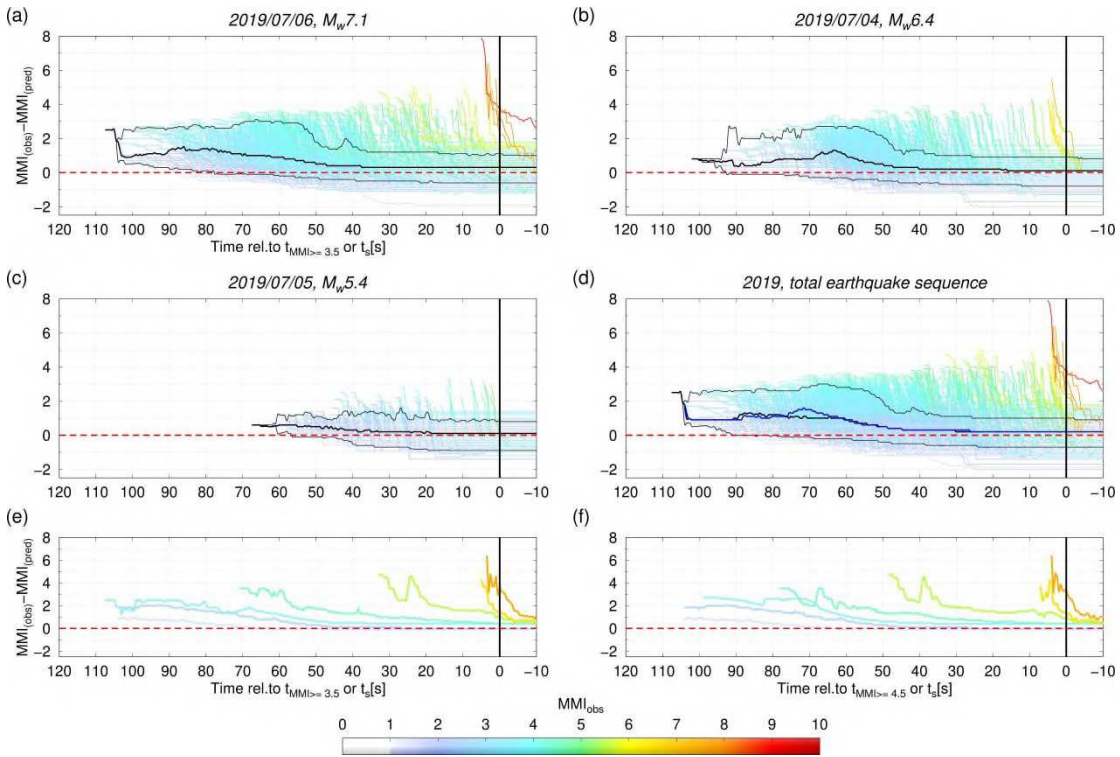
1283

1284

1285

1286

1287



1289

1290 **Fig. 9** (a)-(d), Ground motion prediction errors as a function of warning time for three  
 1291 respective events and the total earthquake sequence. Warning time is defined as the time  
 1292 relative to when the damage threshold is reached for the first time at each individual sites  
 1293 or the theoretical S arrival ( $t_s$ ) for sites with blow-threshold amplitudes. The curves are  
 1294 colored according to the observed peak MMI value for each recording site. Black lines  
 1295 illustrate the 5th, 50th, and 95th percentiles at each point of warning time for alert criterion  
 1296 of  $MMI_{alert} = 3.5$ ; Blue line in figure (d) shows the median warning time for alert criterion of  
 1297  $MMI_{alert} = 2.5$ ,  $MMI_{tw} = 4.5$ . (e)-(f), the medians for each point of warning time are shown  
 1298 for each intensity bin (1.5:1:8.5), the curves are colored according to the corresponding  
 1299 intensity bin.

1300

1301

## Supplementary Files

This is a list of supplementary files associated with this preprint. Click to download.

- [supplementaryinformation.docx](#)